Statistics and Forecasting of Aftershocks during the 2019 Ridgecrest, California, Earthquake Sequence

Robert Shcherbakov[1,1]

[1]Western University

November 30, 2022

Abstract

The 2019 Ridgecrest, California, earthquake sequence represents a complex pattern of seismicity that is characterized by the occurrence of a well defined foreshock sequence followed by a mainshock and subsequent aftershocks. In this work, a detailed statistical analysis of the sequence is performed. Particularly, the parametric modelling of the frequency-magnitude statistics and the earthquake occurrence rate is carried out. It is shown that the clustering of earthquakes plays an important role during the evolution of this sequence. In addition, the problem of constraining the magnitude of the largest expected aftershocks to occur during the evolution of the sequence is addressed. In order to do this, two approaches are considered. The first one is based on the extreme value theory, whereas the second one uses the Bayesian predictive framework. The latter approach has allowed to incorporate the complex earthquake clustering through the Epidemic Type Aftershock Sequence (ETAS) process and the uncertainties associated with the model parameters into the computation of the corresponding probabilities. The results indicate that the inclusion of the foreshock sequence into the analysis produces higher probabilities for the occurrence of the largest expected aftershocks after the M7.1 mainshock compared to the approach based on the extreme value distribution combined with the Omori-Utsu formula for the earthquake rate. Several statistical tests are applied to verify the forecast.

Statistics and Forecasting of Aftershocks during the 2019 Ridgecrest, California, Earthquake Sequence

Robert Shcherbakov[1,2]

[1]Department of Earth Sciences, University of Western Ontario, London, Ontario, *N6A 5B7*, Canada.
[2]Department of Physics and Astronomy, University of Western Ontario, London, Ontario, *N6A 3K7*, Canada.

Key Points:

- Statistical analysis of the 2019 Ridgecrest, California, earthquake sequence is performed.
- The probabilities for the occurrence of the largest expected aftershocks are computed using the Bayesian predictive framework.
- The aftershock forecast is verified retrospectively using several statistical tests.

Corresponding author: Robert Shcherbakov, `rshcherb@uwo.ca`

Abstract

The 2019 Ridgecrest, California, earthquake sequence represents a complex pattern of seismicity that is characterized by the occurrence of a well defined foreshock sequence followed by a mainshock and subsequent aftershocks. In this work, a detailed statistical analysis of the sequence is performed. Particularly, the parametric modelling of the frequency-magnitude statistics and the earthquake occurrence rate is carried out. It is shown that the clustering of earthquakes plays an important role during the evolution of this sequence. In addition, the problem of constraining the magnitude of the largest expected aftershocks to occur during the evolution of the sequence is addressed. In order to do this, two approaches are considered. The first one is based on the extreme value theory, whereas the second one uses the Bayesian predictive framework. The latter approach has allowed to incorporate the complex earthquake clustering through the Epidemic Type Aftershock Sequence (ETAS) process and the uncertainties associated with the model parameters into the computation of the corresponding probabilities. The results indicate that the inclusion of the foreshock sequence into the analysis produces higher probabilities for the occurrence of the largest expected aftershocks after the M7.1 mainshock compared to the approach based on the extreme value distribution combined with the Omori-Utsu formula for the earthquake rate. Several statistical tests are applied to verify the forecast.

Plain Language Summary

Strong earthquakes typically trigger the subsequent sequence of events known as aftershocks. Among those, the largest aftershocks can pose significant hazard and result in additional damage to infrastructure already weakened by the mainshock. Therefore, the estimation of the magnitude of the largest expected aftershock is of critical importance. This problem can be addressed within the statistical modelling of the occurrence of earthquakes. In this work, the 2019 Ridgecrest, California, earthquake sequence is chosen to illustrate and compare several approaches to constrain the magnitudes of the largest expected aftershocks during the evolution of the sequence. The first approach uses the extreme value theory and the modelling of the earthquake rate based on the Omori-Utsu formula. Whereas, the second approach uses a recently formulated method based on the Bayesian predictive analysis and the Epidemic Type Aftershock Sequence (ETAS) model to approximate the earthquake rate. The obtained results indicate that the latter ap-

proach produces statistically accurate forecast for the magnitudes of the largest expected earthquakes. This is verified by applying several statistical tests.

1 Introduction

The occurrence of a significant mainshock presents an opportunity to test different existing or novel statistical approaches to model the evolution of the corresponding sequences of earthquakes that precede and follow the mainshock. Among several statistical measures, the computation of the probability to have the magnitude of the largest expected earthquake to be above a certain value during a predefined future time interval is of critical importance. In this respect, the 2019 Ridgecrest, California, earthquake sequence represents the latest highly productive and non-standard sequence to be analyzed in detail.

The problem of constraining the magnitudes of the largest expected aftershocks is important as these aftershocks can inflict further damage to already weakened by a mainshock structures or the evolution of the sequence can trigger even larger subsequent events (Gerstenberger et al., 2005; Shebalin et al., 2011; Omi et al., 2013; Page et al., 2016). The standard approach is to use the past seismicity to compute the probabilities of having subsequent strong earthquakes during a finite future time interval. The most recognized model was formulated by Reasenberg and Jones (1989) for California based on the analysis of the past aftershock sequences. In that model, the probabilities are computed from the extreme value distribution by assuming that the occurrence of earthquakes follows a non-homogeneous Poisson process, the earthquake rate is approximated by the Omori-Utsu formula and the frequency-magnitude statistics is described by the left-truncated exponential distribution. Reasenberg and Jones (1989) estimated the average values of the model parameters to be used in California. However, a recent work by Hardebeck et al. (2019) introduced improvements to the original model by analysing more recent sequences, introducing the ability to control the early incompleteness of aftershock sequences, and using the Bayesian updating of the model parameters. These developments contributed to the introduction of the operational aftershock forecasting in the U.S. by the U.S. Geological Survey (Michael et al., 2019). A similar approach has been undertaken in Japan to create a real-time system for automatic aftershock forecasting (Omi et al., 2016, 2019). Earthquake forecasting centers also operate in New Zealand (Rhoades et al., 2018) and Italy (Taroni et al., 2018), where the evaluation of earthquake probabilities and assessment of earthquake hazard are routinely performed.

A critical aspect of any earthquake forecasting methods is their prospective/retrospective testing and validation (Kagan & Jackson, 1995). This is consistently implemented by the Collaboratory for the Study of Earthquake Predictability (CSEP) (Schorlemmer et al., 2007; Zechar et al., 2010; Schorlemmer et al., 2018; Gerstenberger et al., 2020). Within the CSEP framework several statistical methods were developed to test the short/long term earthquake forecasts. Those methods test the consistency of a given forecasting scheme to reproduce the observed number of earthquakes, their spatial and magnitude distributions during the forecasting time interval (Zechar et al., 2010). They also incorporate likelihood based approaches to compare various forecasting schemes. For example, this framework was used to test the performance of aftershock forecasts during the 2011 Tohoku, Japan, earthquake (Nanjo et al., 2012), the 2010 Canterbury, New Zealand, earthquake sequence (Rhoades et al., 2016; Cattania et al., 2018), and the 2016 Kaikoura, New Zealand, earthquake sequence (Rhoades et al., 2018).

An early systematic empirical study of aftershocks concluded that the largest occurred aftershock on average was approximately 1.2 magnitude less than the magnitude of a mainshock (Båth, 1965). This is referred to as Båth's law. Subsequently, it was proposed that the difference was independent of the number of events and its mean value was proportional to the inverse of the b-value (Vere-Jones, 1969, 1975). More recent studies have provided further details on this difference (Console et al., 2003; Shcherbakov & Turcotte, 2004; Tahir et al., 2012; Shearer, 2012; Shcherbakov et al., 2013). The aftershock sequences also exhibit scaling with respect to the lower magnitude cutoff (Shcherbakov et al., 2004; Shcherbakov, Turcotte, & Rundle, 2005; Shcherbakov et al., 2006, 2015).

An important limitation of all earthquake catalogs is the early aftershock incompleteness (Kagan, 2004; Peng et al., 2006; Hainzl, 2016b, 2016a). This incompleteness can affect the estimation of the model parameters if the magnitude of completeness is underestimated. As a result, this can significantly influence the calculation of the probabilities for the occurrence of extreme earthquakes. To recover partially the true rate a variable magnitude of completeness can be considered (Helmstetter et al., 2006; Omi et al., 2014; Page et al., 2016). Several approaches were suggested to recover the aftershock rate by using the information of early aftershocks in order to estimate the probability of larger subsequent events during future evolution of the sequences (Omi et al., 2013; Ebrahimian et al., 2014; Omi et al., 2016).

The occurrence of strong earthquakes typically produces spatial and temporal clusters. This clustering is a result of triggering by preceding earthquakes that can lead to a cascade of events with a complicated branching structure (Felzer et al., 2004). To describe such a clustering, the ETAS model was introduced that offers a realistic and quantifiable approximation to the earthquake occurrence rate (Ogata, 1988, 1999, 2017). Particularly, it can model the rate of earthquakes punctuated by the occurrence of strong earthquakes. This also allows to quantify the increased earthquake hazard after a mainshock by incorporating the triggering ability of foreshocks, a mainshock, and subsequent aftershocks. It also can be used for short-term forecasting of large earthquakes by studying past seismicity (Helmstetter et al., 2006; Werner et al., 2011; Ogata, 2017; Ebrahimian & Jalayer, 2017; Harte, 2017; Omi et al., 2019).

After the occurrence of the 2019 Ridgecrest earthquakes, several approaches have been used to study the statistical and triggering aspects of this sequence. The operational earthquake forecasting was documented based on the UCERF3-ETAS model (Milner et al., 2020; Savran et al., 2020). Retrospective analysis of the historic seismicity in California and its relation to the initiation of the 2019 Ridgecrest sequence was performed (Ogata & Omi, 2020). Predictive skills of the models based on the Coulomb stress transfer were analyzed (Mancini et al., 2020; Toda & Stein, 2020). The triggering of aftershocks during the evolution of the sequence was studied using the stress-similarity model (Hardebeck, 2020). The question of changes in the stress field inferred from past seismicity and its relation to the initiation of the Ridgecrest sequence and subsequent relaxation was addressed in Nanjo (2020).

In this paper, a detailed statistical analysis of the 2019 Ridgecrest earthquake sequence was performed to study its temporal evolution and frequency-magnitude statistics. In addition, several methods were considered to estimate the probabilities to have the largest expected aftershock to be above a certain magnitude during several stages of the evolution of the sequence. The computation of probabilities was performed using two approaches, i.e., the one based on the extreme value theory and the second one using the Bayesian predictive distribution. These approaches assume parametric models for the earthquake occurrence rate and the frequency-magnitude statistics. Specifically, the Omori-Utsu (OU) law (Omori, 1894; Utsu, 1961; Utsu et al., 1995), the compound Omori-Utsu law (Ogata, 1983), and the Epidemic Type Aftershock Sequence (ETAS) process (Ogata, 1988, 1999, 2017) were used to approximate the earthquake rate. The frequency-magnitude statistics of earthquakes was modelled by the left-truncated exponential distribution (Vere-Jones, 2010). The obtained results, which are reported below, suggest that the clustering of earthquakes plays an important role in approximating the earthquake rate and as a consequence can significantly affect the computation of the probabilities for the occurrence of the largest expected aftershocks.

The paper is organized as follows. In Section 2, the statistical methods used in the study are summarized and explained. In Section 3, a detailed analysis of the sequence is presented. The retrospective validation of the forecasting results is given in Section 4. In Section 5, the obtained results are summarized and evaluated. The last section presents concluding remarks.

2 Data and Methods

2.1 The 2019 Ridgecrest earthquake sequence

The 2019 Ridgecrest earthquake sequence started on July 4th when several small events of low magnitude occurred not far away from the town of Ridgecrest in California. Then, two strong foreshocks of magnitudes M3.98 and M6.4 struck on 2019/07/04 at 17:02:55 UTC and 17:33:49 UTC, respectively (Figure 1). These events were followed by a well-developed aftershock sequence that culminated in the occurrence of M7.1 mainshock on 2019/07/06 (03:19:53 UTC), which in turn generated a more prolific aftershock sequence. The M6.4 foreshock ruptured several predominantly strike-slip, left-lateral fault segments, whereas the M7.1 mainshock occurred on a system of several right-lateral fault segments conjugate to the rupture of the M6.4 foreshock (Ross et al., 2019; Barnhart et al., 2019). Many of the foreshocks and subsequent aftershocks of the M7.1 mainshock occurred on numerous secondary faults adjacent to the main rupture faults. It was suggested that this earthquake sequence occurred in an immature fault zone with a complex fault structure (Ross et al., 2019; Liu et al., 2019).

To analyze the 2019 Ridgecrest earthquake sequence, the earthquake catalog provided by the Southern California Seismic Network (SCSN, 2020) was used. The spatial distribution of seismicity during 14 days starting from 2019/07/04 (17:02:55 UTC) is shown

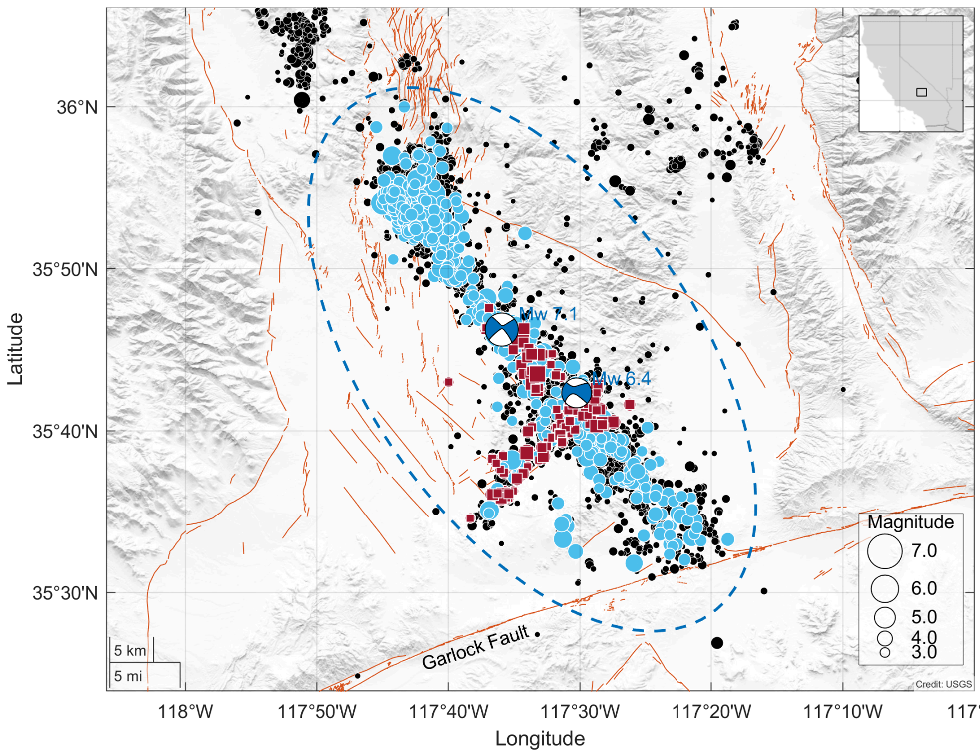

Figure 1. The distribution of earthquake epicentres of the 2019 Ridgecrest, California, sequence during 14 days starting from 2019/07/04 (17:02:55 UTC). Dark red solid squares within an elliptical zone indicate foreshocks above magnitude $m \geq 3.2$ during 1.428 days before the occurrence of the M7.1 mainshock on 2019/07/06 (03:19:53 UTC). Similarly, blue solid circles indicate aftershocks of the M7.1 mainshock. The focal mechanisms of the M7.1 mainshock and M6.4 foreshock are plotted as beach balls. All other earthquakes above magnitude $m \geq 2.0$ are shown as black solid circles. The quaternary faults are plotted as light brown line segments.

in Figure 1. This includes the occurrence of the M6.4 foreshock on 2019/07/04 (17:33:49 UTC) and the occurrence of the M7.1 mainshock on 2019/07/06 (03:19:53 UTC). Their focal mechanisms are also shown and were obtained from the SCSN Moment Tensor catalog (SCSN, 2020). The foreshock-aftershock zone for the sequence is defined as an elliptical region outlining the majority of earthquakes that occurred near the ruptures of both the M6.4 foreshock and M7.1 mainshock. Figure 1 also shows the quaternary faults for this region extracted from the U.S.G.S. Quaternary fault and fold database (USGS, 2006).

When analyzing seismicity, several time intervals, during which the parameters of statistical models can be estimated or future evolution of the seismicity can be quantified, are defined. Specifically, the past seismicity is extracted during the *training time interval* $[T_0, T_e]$. To minimize the effect of earlier earthquakes in the sequence, the training time interval is typically subdivided into a preparatory time interval $[T_0, T_s]$ and a *target time interval* $[T_s, T_e]$ during which the parameters of the earthquake models are estimated. One also considers a *forecasting time interval* $[T_e, T_e + \Delta T]$ during which specific measures of seismicity can be computed or evolution of seismicity can be forecasted. For properly estimating the parameters of earthquake models, it is also important to consider the seismicity above the magnitude of completeness m_c as typical earthquake catalogs have missing events below this magnitude.

For the statistical modeling of seismicity, the occurrence of earthquakes can be considered as a realization of a stochastic marked point process in time (Daley & Vere-Jones, 2003; Vere-Jones, 2010). In this representation, the earthquakes are characterized by their occurrence times t_i and magnitudes m_i represent corresponding marks. The occurrence of earthquakes during a specified time interval can be arranged in an ordered set $\mathbf{S} = \{(t_i, m_i)\} : i = 1, ..., n$. In one simplified assumption, the occurrence of earthquakes in the sequence can be described by a non-homogeneous Poisson marked point process (Utsu et al., 1995; Shcherbakov, Yakovlev, et al., 2005), where magnitudes and the time intervals between successive events are not correlated.

2.2 Exponential Distribution and the Gutenberg-Richter Scaling Relation

The frequency-magnitude statistics of earthquake magnitudes is typically modelled by the left-truncated exponential distribution (Vere-Jones, 2010):

$$f_\theta(m) = \beta \exp\left[-\beta\left(m - m_0\right)\right] , \tag{1}$$

$$F_\theta(m) = 1 - \exp\left[-\beta\left(m - m_0\right)\right] , \qquad \text{for} \quad m \geq m_0 , \tag{2}$$

where $f_\theta(m)$ is the probability density, $F_\theta(m)$ is the cumulative distribution function, and $\theta = \{\beta\}$ is the model parameter. m_0 is a given lower magnitude cutoff set above the catalog completeness level $m_0 \geq m_c$. All earthquakes above m_0 during the target time interval $[T_s, T_e]$ are used to estimate the model parameter β.

The parameter β is related to the b-value of the Gutenberg-Richter (GR) scaling relation, $\beta = \ln(10)b$ (Gutenberg & Richter, 1944):

$$\log_{10} N\left(\geq m\right) = a - b\, m , \tag{3}$$

where $N\left(\geq m\right)$ is the cumulative number of earthquakes above magnitude m. The GR relation combines two aspects of the occurrence of earthquakes, i.e. the frequency-magnitude statistics of earthquake magnitudes and the average rate of the occurrence of earthquakes, which is quantified through the parameter a. $N\left(\geq 0\right) = 10^a$ gives the total number of earthquakes above magnitude zero that occurred during the corresponding time interval.

The standard method to estimate the parameter β (or b-value) is to use the maximum likelihood approach, which has an analytic solution for the point estimator of the parameter of the exponential distribution. However, in typical earthquake catalogs the magnitudes are binned and not continuous variables. Therefore, one needs to apply a corrected estimator, which explicitly assumes the binning of the magnitudes (Bender, 1983). For the estimation of the parameter uncertainties at a given confidence level in case of binned magnitudes one can use the method suggested in Tinti and Mulargia (1987).

2.3 Omori-Utsu Law

The occurrence of moderate to large earthquakes, in most cases, triggers subsequent aftershock sequences and results in the rise of seismic activity. The most accepted model that reproduces the rate of the occurrence of aftershocks is know as the Omori-Utsu (OU) law (Omori, 1894; Utsu, 1961; Utsu et al., 1995):

$$\lambda_\omega(t) = \frac{K_\mathrm{o}}{(t + c_\mathrm{o})^{p_\mathrm{o}}} , \tag{4}$$

where λ_ω is the rate of aftershocks per unit time for events above a certain magnitude m_0. $\omega = \{K_\mathrm{o}, c_\mathrm{o}, p_\mathrm{o}\}$ are the OU model parameters. The time t is elapsed since $T_0 = 0$, which corresponds to the time of the occurrence of the mainshock. The parameter K_o describes the productivity of the sequence, c_o is a characteristic time, and p_o specifies how fast or slow the sequence decays in time. The parameters can be estimated using the maximum likelihood method and parameter uncertainties are computed using the inverse of the Fisher information matrix, which is derived from the likelihood function (Ogata, 1983, 1999). In this model, it is assumed that the occurrence of earthquakes can be approximated by a non-homogeneous Poisson process, where earthquake magnitudes are independent and identically distributed (i.i.d.) random numbers and do not influence the future earthquake rate. The Bayesian approach to estimate the parameters and their uncertainties of the OU law was also implemented (Holschneider et al., 2012).

The Omori-Utsu law is applicable to "standard" aftershock sequences with a single mainshock and a consistently decaying rate. However, in some cases the earthquake sequence can be punctuated by several strong shocks each one of them producing their own aftershocks. In that case, a compound Omori-Utsu model can be considered (Ogata, 1983; Shcherbakov et al., 2012). In a case of two strong earthquakes, it is written as:

$$\lambda_\omega(t) = \frac{K_1}{(t + c_1)^{p_1}} + H(t - \tau_\mathrm{m}) \frac{K_2}{(t - \tau_\mathrm{m} + c_2)^{p_2}} , \tag{5}$$

where $\omega = \{K_1, c_1, p_1, K_2, c_2, p_2\}$, time t is elapsed since the occurrence of the first event at $T_0 = 0$ and τ_m is the time of the occurrence of the second strong event. $H(x)$ is a Heaviside step function and is equal to one for positive $x \geq 0$ and is zero otherwise. For the times past the occurrence of the second strong earthquake ($t \geq \tau_\mathrm{m}$), Eq. (5) defines the earthquake rate as a superposition of two aftershock sequences triggered by the both strong earthquakes.

2.4 Epidemic Type Aftershock Sequence (ETAS) Model

The occurrence of earthquakes is characterized by the clustering of seismicity. This clustering is a direct manifestation of the ability of earthquakes to trigger subsequent events. The ETAS model was introduced to reflect this essential aspect of the occurrence of earthquakes (Ogata, 1988, 1999, 2017). In the temporal version of the model, the conditional earthquake rate $\lambda_\omega(t|\mathcal{H}_t)$ at a given time t is given as (Ogata, 1988; Harte, 2010):

$$\lambda_\omega(t|\mathcal{H}_t) = \mu + K \sum_{i:t_i<t}^{N_t} \frac{e^{\alpha(m_i - m_0)}}{\left(\frac{t-t_i}{c} + 1\right)^p}\,, \tag{6}$$

where $\omega = \{\mu,\, K,\, c,\, p,\, \alpha\}$ is a set of parameters and m_0 is a reference magnitude. The summation is performed over the history, $\mathcal{H}_t$, of past events up to time t during the time interval $[T_0,\, t]$. N_t is the number of earthquakes in the interval $[T_0,\, t]$ above the lower magnitude cutoff m_0. In the ETAS process, a certain fraction of earthquakes occurs randomly with a constant rate μ. These earthquakes are associated with background seismicity driven by tectonic loading and can be modelled as a homogeneous Poisson process. It is also postulated that each earthquake is capable of triggering its own offsprings. As a result, the total earthquake rate at a given time, is a superposition of the background rate given by μ and the contribution from each already occurred earthquake.

As the ETAS rate, Eq. (6), is conditioned on past seismicity $\mathcal{H}$, one has to minimize the effect of lack of earthquakes at the start of the sequence when estimating the ETAS parameters. For this, one can consider a short time interval $[T_0,\, T_s]$ before the target time interval $[T_s,\, T_e]$. The earthquakes in the interval $[T_0,\, T_s]$ can be used to properly estimate the conditional earthquake rate during the target time interval $[T_s,\, T_e]$. The explicit forms of the log-likelihood function and the productivity of the ETAS model were given in Shcherbakov et al. (2019). The ETAS parameters $\omega = \{\mu,\, K,\, c,\, p,\, \alpha\}$ are estimated in the target time interval $[T_s,\, T_e]$ by maximizing the likelihood function and the uncertainties are computed using the inverse of the Fisher information matrix.

2.5 Extreme Value Distribution

For the sequence of earthquake that can be described as a non-homogeneous Poisson process, the probability that the magnitude of the largest expected event will exceed m for all possible number of events during a future time interval $[T_e,\, T_e{+}\Delta T]$ can be computed from the extreme value distribution (EVD) (Campbell, 1982; Coles, 2001; Daley & Vere-Jones, 2003):

$$P_{\mathrm{EV}}(m_{\mathrm{ex}} > m|\theta, \omega, \Delta T) = 1 - \exp\{-\Lambda_\omega(\Delta T)\,[1 - F_\theta(m)]\}\,, \tag{7}$$

where the productivity is $\Lambda_\omega(\Delta T) = \int_{T_e}^{T_e+\Delta T} \lambda_\omega(t)\,dt$. Using the exponential model for the magnitude distribution, Eq. (2), this results in the Gumbel distribution for the magnitudes of extreme earthquakes:

$$P_{\mathrm{EV}}(m_{\mathrm{ex}} > m|\theta, \omega, \Delta T) = 1 - \exp\{-\Lambda_\omega(\Delta T)\, \exp\left[-\beta\,(m - m_0)\right]\}\,. \tag{8}$$

Assuming that the earthquake rate is described by the OU law (4), the productivity $\Lambda_\omega(\Delta T)$ can be computed explicitly and takes the following form for $p_{\mathrm{o}} \neq 1$:

$$\Lambda_\omega(\Delta T) = K_{\mathrm{o}} \frac{\left(T_e + c_{\mathrm{o}}\right)^{1-p_{\mathrm{o}}} - \left(T_e + \Delta T + c_{\mathrm{o}}\right)^{1-p_{\mathrm{o}}}}{p_{\mathrm{o}} - 1}\,. \tag{9}$$

Given a set of parameters $\{\theta,\, \omega\}$, which can be estimated from past seismicity during the training time interval $[T_s,\, T_e]$, Eqs. (8) and (9) allow to compute the probability to have the extreme earthquake above magnitude m during a future time interval ΔT. It is equivalent to the computation of the probabilities given in Reasenberg and Jones (1989).

For the compound OU model (5) the productivity $\Lambda_\omega(\Delta T)$ can be expressed as follows for $p_1 \neq 1$ and $p_2 \neq 1$:

$$\begin{aligned} \Lambda_\omega(\Delta T) \;=\; & K_1\, \frac{(T_e + c_1)^{1-p_1} - (T_e + \Delta T + c_1)^{1-p_1}}{p_1 - 1} + \\ & K_2\, \frac{(T_e - \tau_{\mathrm{m}} + c_2)^{1-p_2} - (T_e + \Delta T - \tau_{\mathrm{m}} + c_2)^{1-p_2}}{p_2 - 1}\,, \end{aligned} \tag{10}$$

where τ_{m} is the time of the occurrence of the second strong earthquake during the training time interval $[T_s,\, T_e]$.

2.6 Bayesian Predictive Distribution

The computation of the EVD (7) using specific parametric models for the earthquake rate and frequency-magnitude statistics, requires the knowledge of the model parameters. However, the true values of the model parameters are not known for specific earthquake sequences. As a result, the parameter estimates are used, which are computed with a given range of uncertainties. Those uncertainties can significantly affect the computation of the corresponding probabilities. The incorporation of the model uncertainties into the computation of probabilities can be achieved through the Bayesian predictive distribution (BPD) (Zöller et al., 2013; Shcherbakov et al., 2018, 2019). The BPD for the largest expected event m_{ex} to be greater than a certain value m and during the forecasting time interval ΔT is:

$$P_{\mathrm{B}}(m_{\mathrm{ex}} > m|\mathbf{S}, \Delta T) = \int\limits_{\Omega}\int\limits_{\Theta} P_{\mathrm{EV}}(m_{\mathrm{ex}} > m|\theta, \omega, \Delta T)\, p(\theta, \omega|\mathbf{S})\, d\theta\, d\omega\,, \tag{11}$$

where Θ and Ω define the multidimensional domains of the frequency-magnitude distribution and earthquake rate parameters, respectively. When computing the predictive distribution, Eq. (11), the model parameter uncertainties are fully integrated into the BPD (Renard et al., 2013; Shcherbakov et al., 2019). This is done through the use of the posterior distribution function $p(\theta, \omega|\mathbf{S})$, which characterizes the distribution of the model parameter uncertainties.

For the ETAS model, the extreme value distribution for the extreme events does not follow Eq. (7), due to stochastic nature of the process, which deviates from a non-homogeneous Poisson process. In this case, one can compute the extreme value distribution by stochastic simulation of the ETAS model and extracting the maximum magnitude from each simulated sequence (Shcherbakov et al., 2019).

To compute the BPD (11) for a given training time interval, first, the Markov Chain Monte Carlo (MCMC) sampling of the posterior distribution is performed to generate a chain of the ETAS parameters using the Metropolis-within-Gibbs algorithm. The generated chains of length $N_{\rm sim}$ are used to simulate the ensemble of the ETAS processes forward in time during the forecasting time interval ΔT. From each simulated sequence the maximum event is extracted and the distribution of these maxima approximates the BPD (Shcherbakov et al., 2019).

3 Results

3.1 Frequency-Magnitude Statistics

The earthquakes within an elliptical region, given in Figure 1, were extracted during predefined target time intervals. The frequency-magnitude statistics of earthquake magnitudes were computed for the foreshock sequence starting from 2019/07/04 (17:02:55 UTC) which corresponds to $T_0 = 0$ and during the target time interval $[T_s, T_e] = [10^{-4}, 1.428]$ days. It was also computed for the aftershocks of the M7.1 mainshock starting from 2019/07/06 (03:19:53 UTC) during 7 days after the mainshock. The frequency-magnitude statistics was also computed for the whole sequence including both foreshocks and aftershocks during 31 days. The results are given in Figure 2 as open symbols for events larger than $m \geq 2.0$. The maximum likelihood fits of the exponential distribution, Eq. (2), to the frequency-magnitude data above $m \geq 3.2$ are shown as GR plots with estimated b-values using

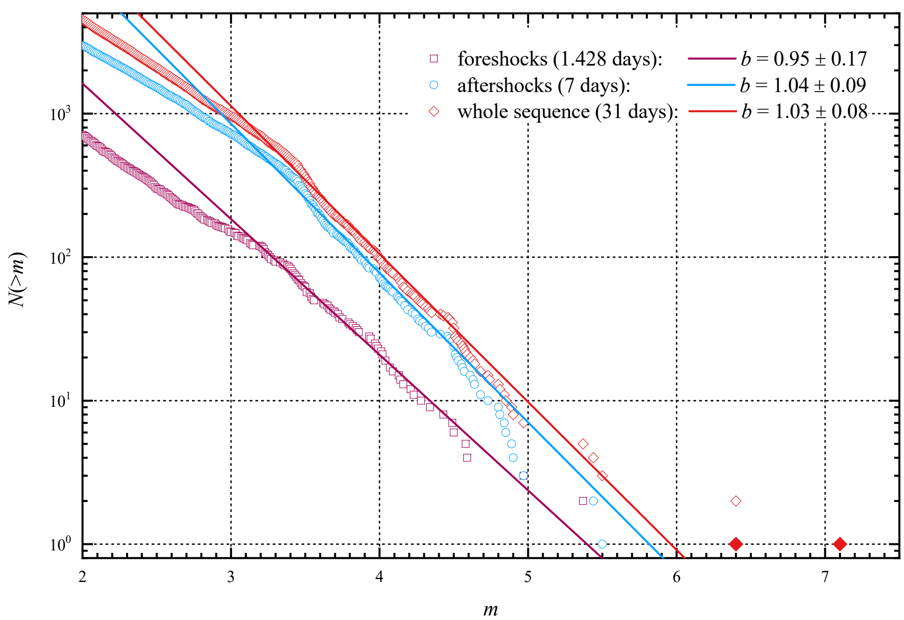

Figure 2. The frequency-magnitude statistics of earthquakes in the sequence and the modelling by the Gutenberg-Richter relation, Eq. (3). The symbols (representing the cumulative numbers) correspond to the foreshocks of the M7.1 mainshock (open squares), the aftershocks of the mainshock (open circles), and for the whole sequence (open diamonds). The fits of the GR relation are plotted as straight lines. The estimated b-values are given in the legend for all earthquakes above $m \geq 3.2$. The uncertainties are given as 95% confidence intervals.

the method of Bender (1983) and their 95% confidence intervals according to Tinti and Mulargia (1987).

The sequence exhibited a change in the slope of the frequency-magnitude statistics around a magnitude 3.2. This was the reason to use only the events above this value in the analysis. This change in the behavior can be the result of the early aftershock incompleteness observed right after the M6.4 foreshock and the M7.1 mainshock or it can be related to the fact that the aftershocks occurred on a distributed fault network and the geometrical distribution of fault sizes affected the statistics of earthquake magnitudes. The fit of the exponential distribution, Eq. (2), (or the corresponding Gutenberg-Richter relation) to the frequency-magnitude statistics of the foreshock and aftershock sequences produced the b-values which were typical for tectonic earthquakes as illustrated in Figure 2. The largest aftershock of the M7.1 mainshock had a magnitude 5.5 and occurred less than half an hour after the mainshock. Two more strong aftershocks of magnitude

4.7 and 5.0 occurred later in the sequence on 20th and 48th days after the mainshock. The value of the largest occurred aftershock is lower than what would be expected from Båth's law (Båth, 1965). It is possible that the M6.4 foreshock partially released the accumulated strain energy in the region and this resulted in a lower magnitude of the largest occurred aftershock.

3.2 Earthquake Rate Evolution and Modelling

First, the earthquake rate was modelled separately for the foreshock and aftershock sequences using the OU law (4). The results are given in Figure 3 for all earthquakes above magnitude $m \geq 3.2$. For the foreshock sequence, the following target time interval was used $[T_s, T_e] = [10^{-3}, 1.407]$ days with $T_0 = 0$ corresponding to 2019/07/04 (17:33:49 UTC). For the aftershock sequence, $T_0 = 0$ was set to the occurrence of the M7.1 mainshock on 2019/07/06 (03:19:53 UTC) with the target time interval $[T_s, T_e] = [10^{-3}, 30]$ days. The OU law parameters for the foreshock and aftershock sequences are given in the legend with the corresponding 95% confidence intervals. The earthquake decay rates after the M6.4 foreshock and M7.1 mainshock exhibited a consistent pattern observed in other prominent aftershock sequences. The fit of the OU law (4) produced $p = 0.99 \pm 0.18$ for the foreshock sequence and $p = 1.28 \pm 0.07$ for the aftershock sequence (Figure 3). The smaller p-value for the foreshock sequence can be the result of a strong M5.36 foreshock that occurred 16.2 hours before the M7.1 mainshock and triggered its own sequence of events.

Next, the compound OU model (5) was used to fit the sequence starting from the occurrence of the M6.4 foreshock on 2019/07/04 (17:33:49 UTC) corresponding to $T_0 = 0$ and during the following target time interval $[T_s, T_e] = [10^{-3}, 8.407]$ days. This is illustrated in Figure 4 and Figure S1. The maximum likelihood fitting of the compound OU model yielded the following parameters $\{K_1, c_1, p_1, K_2, c_2, p_2\} = \{23.22, 0.0026, 0.93, 40.3, 0.034, 1.59\}$.

The ETAS model (6) was fitted to the 2019 Ridgecrest sequence using a number of target time intervals. In one particular example, the training time interval $[T_s, T_e] = [0.03, 8.428]$ days was used with $T_0 = 0$ corresponding to the start date 2019/07/04 (17:02:55 UTC). The estimated conditional rate, Eq. (6), and the corresponding earthquake magnitudes above $m \geq 3.2$ are plotted in Figure 5 and Figure S2. For comparison, the sep-

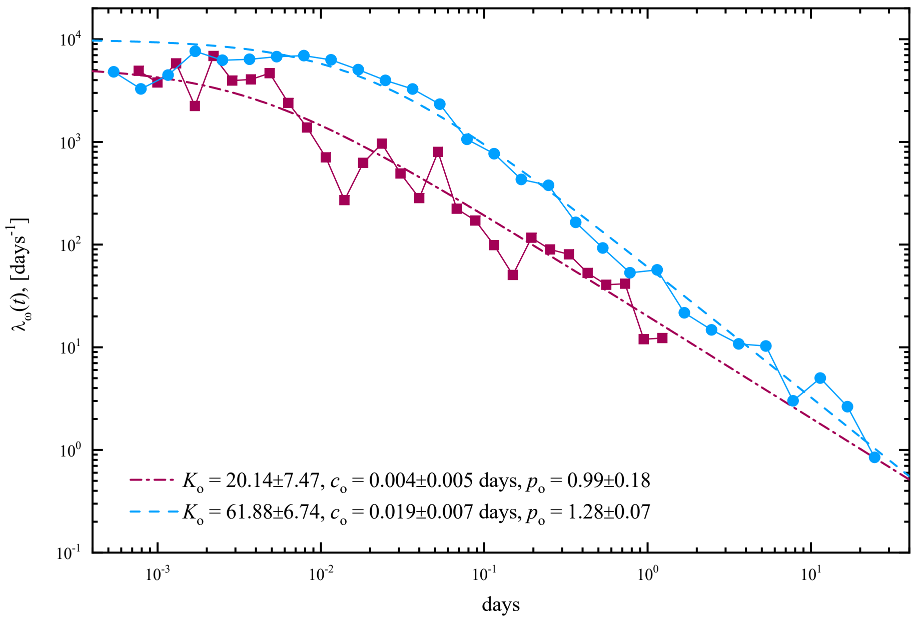

Figure 3. The earthquake decay rates for the foreshock sequence (solid squares) and for the aftershock sequence (solid circles). The corresponding fits of the Omori-Utsu law, Eq. (4), to the foreshock (dash-dotted line) and aftershock (dashed line) sequences. The estimated parameters with the corresponding 95% confidence intervals are given in the legend.

arate fits of the Omori-Utsu law to the foreshocks and aftershocks of the M7.1 mainshock are also plotted with the parameters given in Figure 3.

Finally, the point estimates of the model parameters and their 95% confidence intervals were computed at predefined times during the evolution of the sequence (Figure 6). The reported b-value at time 1.428 days corresponds to the foreshock sequence starting from the occurrence of the M3.98 event on 2019/07/04 (17:02:55 UTC). The frequency-magnitude statistics and the fitting of the GR relation to the foreshock sequence is also illustrated in Figure 2. The subsequent estimates of b-values at days 1d, 2d, etc., correspond to the time duration of the aftershock sequence since the M7.1 mainshock (Figure 6a). Similarly, the parameters of the OU law (4) were estimated during the same time intervals (Figure 6b). In addition, the point estimates of the ETAS model parameters were also computed (Figure 6c). The parameter μ was held constant at $\mu = 0.05$ to improve the stability of the parameter estimation. It was assumed that the background seismicity rate for earthquakes above magnitude $m \geq 3.2$ was relatively low in this region prior to the start of the sequence.

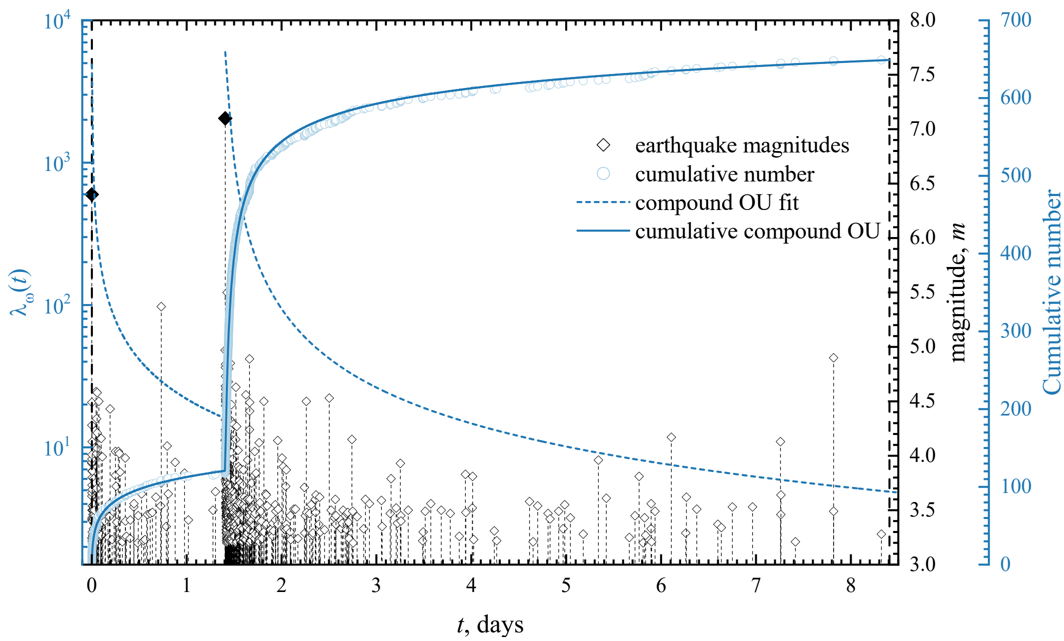

Figure 4. The occurrence of earthquakes during the evolution of the 2019 Ridgecrest sequence and the fitting of the compound Omori-Utsu law, Eq. (5). $T_0 = 0$ corresponds to the occurrence of M6.4 foreshock on 2019/07/04 (17:33:49 UTC). The earthquake magnitudes are plotted as open diamond symbols. The cumulative number of earthquakes is plotted as open circles. The dashed curve corresponds to the fit of the compound Omori-Utsu law, Eq. (5). The corresponding fit of the cumulative numbers is given as a solid curve.

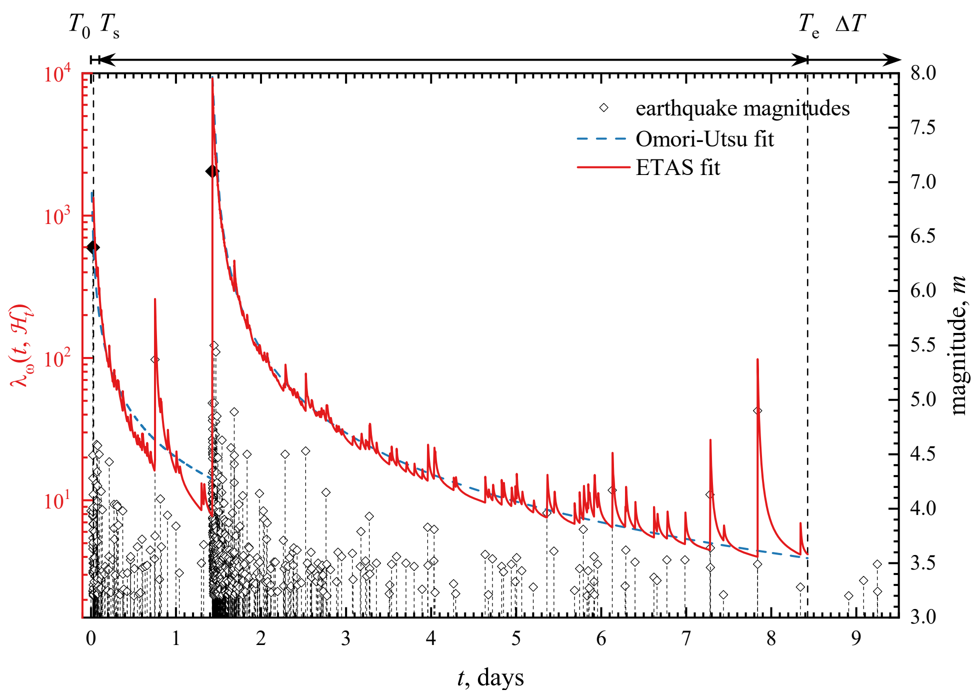

Figure 5. The occurrence of earthquakes during the evolution of the 2019 Ridgecrest sequence and the fitting of the ETAS model, Eq. (6). The start of the sequence $T_0 = 0$ corresponds to the time of the occurrence of the M3.98 foreshock on 2019/07/04 (17:02:55 UTC). The ETAS model is fitted to the sequence during the target time interval $[T_s, T_e] = [0.03, 8.428]$ days. The estimated conditional earthquake rate (solid curve) is plotted using the following ETAS parameters: $\mu = 0.05$, $K = 2.64$, $c = 0.015$, $p = 1.41$, and $\alpha = 2.10$. For comparison, the Omori-Utsu law fit, Eq. (4), is plotted as a short-dashed curve.

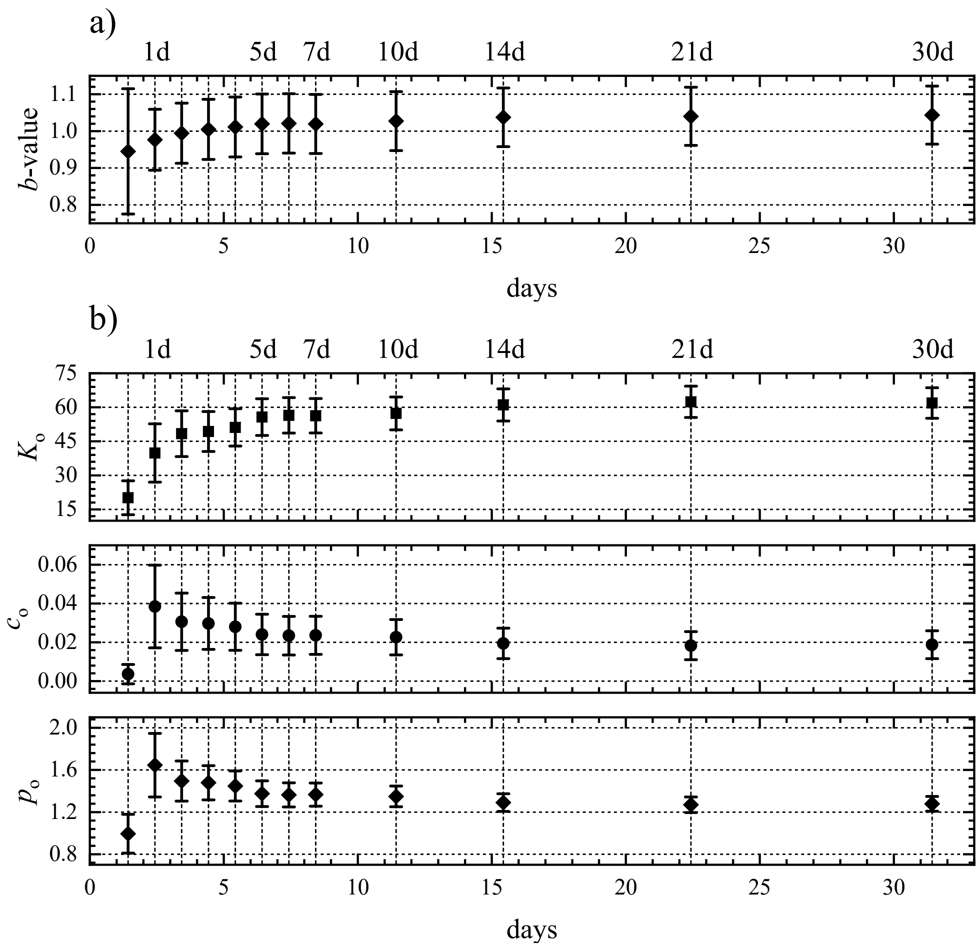

Figure 6. Point estimates of the model parameters during the evolution of the 2019 Ridgecrest sequence. The start of the sequence $T_0 = 0$ corresponds to the time of the occurrence of the M3.98 foreshock on 2019/07/04 (17:02:55 UTC). All the events above magnitude $m \geq 3.2$ were used to compute the parameters using the maximum likelihood method. The point estimates of a) the b-value; b) the Omori-Utsu parameters, Eq. (4), and c) the ETAS parameters, Eq. (6), are plotted. The 95% confidence intervals are also given. The vertical dashed lines correspond to the times in days since the occurrence of the M7.1 mainshock.

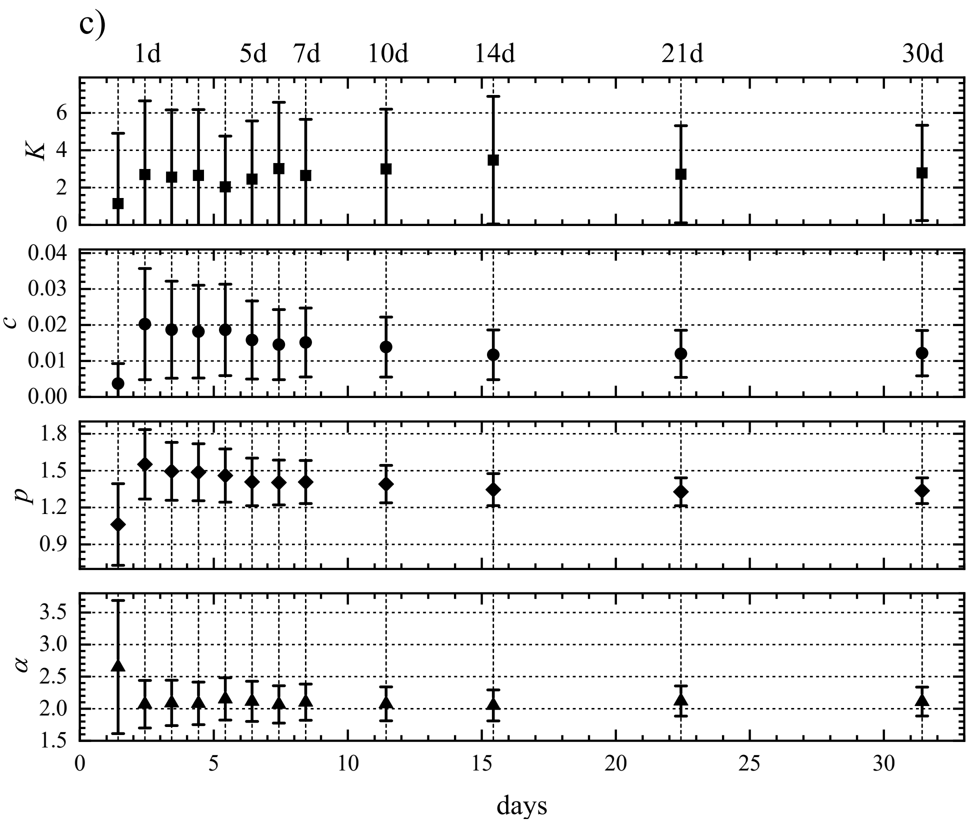

Figure 6. Continued.

3.3 Forecasting the Magnitude of the Largest Expected Earthquake

The EVD (7) and the BPD (11) were used to compute retrospectively the probabilities of having the largest expected earthquakes to occur during predefined times of the evolution of the 2019 Ridgecrest earthquake sequence. This was done both before and after the occurrence of the M7.1 mainshock using the OU (4), compound OU (5), or ETAS (6), parametric models for the earthquake rate and the exponential distribution, Eq. (2), for the distribution of earthquake magnitudes. When computing the probabilities for the aftershock sequence generated by the M7.1 mainshock two cases were analyzed. In the first consideration, only the aftershocks were used. However, when using the ETAS model and the compound OU model the foreshock sequence was also incorporated into the analysis.

First, the only aftershocks of the M7.1 mainshock were used to compute the probabilities of having the strongest aftershocks above a specified magnitude during a future time interval of $\Delta T = 7$ days. The occurrence of the M7.1 mainshock on 2019/07/06 (03:19:53 UTC) corresponded to $T_0 = 0$ with the target time interval $[T_s, T_e] = [10^{-4}, 1]$ days. One particular example is given in Figure 7, where the EVD (8) was computed after 1 day and plotted as a short dashed violet curve. The following model parameter estimates were used: $\{\beta, K_\mathrm{o}, c_\mathrm{o}, p_\mathrm{o}\} = \{2.28, 39.85, 0.038, 1.65\}$. The corresponding probabilities to have strong aftershocks above $m_\mathrm{ex} \geq 5.0$, 6.1, 7.1 are also given.

Next, the BPD (11) was computed using the aftershocks of the M7.1 mainshock during different training time intervals to forecast the magnitudes of the largest expected earthquakes to occur during the evolution of the sequence. The OU law (4) was used to approximate the earthquake rate. The exponential distribution, Eq. (2), was used to model the frequency-magnitude statistics. The forecasting time interval was fixed at $\Delta T = 7$ days. The computed BPD to estimate probabilities for the largest expected aftershocks above magnitude $m \geq 3.2$ during one day after the mainshock is plotted in Figure 7 as a dash-dotted cyan curve. This was done by employing the MCMC sampling of the posterior distribution and the Gamma distribution for the priors of the model parameters (Shcherbakov et al., 2019). The total number of 200,000 MCMC sampling steps were performed for each model. The first 100,000 steps were discarded as "burn in" and the remaining $N_\mathrm{sim} = 100,000$ sampling steps were used for the synthetic model simulations or analysis. For the OU model, this is given in Figure S3. The distribution of

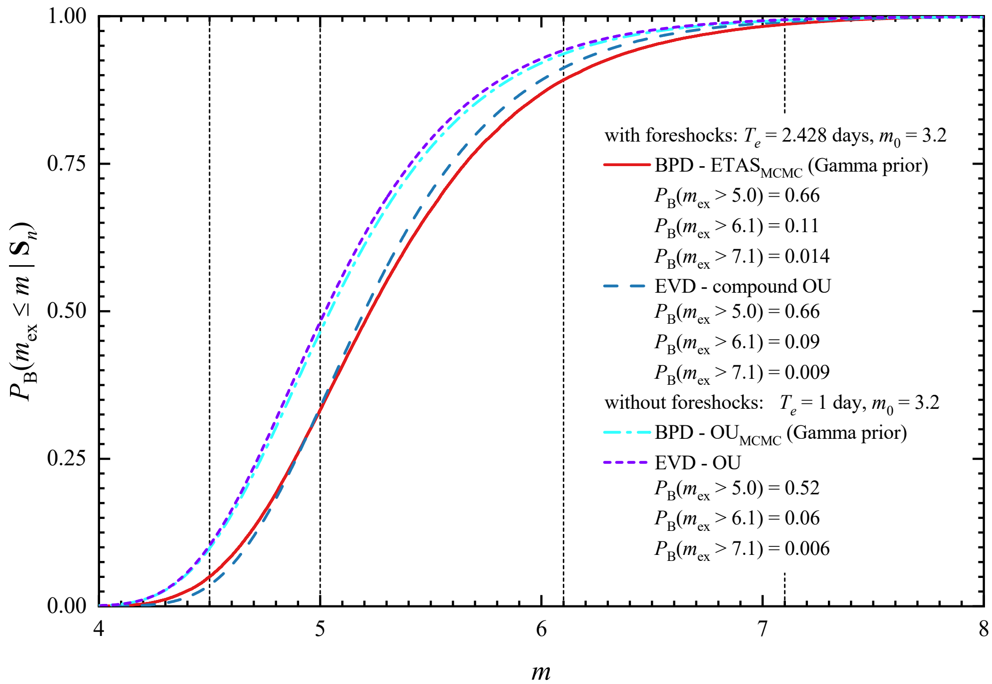

Figure 7. The extreme value and the Bayesian predictive distributions for the 2019 Ridgecrest sequence. The BPD is shown as a solid red curve using the ETAS model and MCMC sampling with the Gamma prior for the foreshocks and 1 day of aftershocks after the M7.1 mainshock. For the same sequence of events, the EVD using the compound OU law is shown as a dashed blue curve. For the rest of the distributions, 1 day of aftershocks after the M7.1 mainshock was used: the OU rate using the MCMC sampling with the Gamma prior (dash-dotted cyan curve); the Gumbel distribution with OU rate (short dashed violet curve).

the OU model parameters computed from the MCMC chain is illustrated in Figure S4. The matrix plot of the pairs of the OU model parameters is given in Figure S5. The values for the mean and variance of the prior distribution (Gamma) of the OU model parameters are provided in Table S1.

To investigate the influence of the foreshocks on the computation of the probabilities for the largest expected aftershocks, the EVD (8) using the compound OU law (5) and the BPD using the ETAS model (6) were computed for the earthquake sequence starting from the occurrence of the first M3.98 foreshock on 2019/07/04 (17:02:55 UTC). The earthquakes above magnitude $m \geq 3.2$ were used. In case of the BPD with the ETAS model, the target time interval $[T_s, T_e] = [0.03, 2.428]$ days was used with $T_0 = 0$ corresponding to 2019/07/04 (17:02:55 UTC), which included the foreshocks and one day of aftershocks after the M7.1 mainshock. The values for the mean and variance of the prior distribution (Gamma) of the compound OU and ETAS model parameters are provided in Tables S2-S3. The resulting BPD is plotted as a solid red curve in Figure 7. The probabilities of having the largest expected earthquakes during the next $\Delta T = 7$ days are provided in the legend. For the same sequence, the EVD (8) with the compound OU law (10) was computed and the corresponding probabilities to have the largest aftershocks during the next $\Delta T = 7$ days were estimated. This is plotted as a dashed blue curve in Figure 7. The MCMC sampling steps are given in Figure S6. The distribution of the compound OU model parameters computed from the MCMC chain is illustrated in Figure S7. The matrix plot of the pairs of the compound OU model parameters is given in Figure S8.

The probabilities to have the largest expected earthquake above a certain magnitude can be computed at specified times during the evolution of the sequence. This can be done by increasing progressively the upper limit T_e of the target time interval $[T_s, T_e]$ for a fixed forecasting interval ΔT. Figure 8 illustrates the computed probabilities from the BPD (11) with the ETAS model (6) for the earthquake rate, and the exponential distribution, Eq. (2), for the frequency-magnitude statistics. $T_0 = 0$ corresponded to the date 2019/07/04 (17:02:55 UTC) and $T_s = 0.03$ days. The MCMC sampling steps, the distribution of the ETAS model parameters, and the matrix plot of the pairs of the ETAS parameters are given in Figures S9-S11 for the following target time interval $[T_s, T_e] = [0.03, 2.4284]$ days. The probabilities were estimated for the largest expected earthquakes to be above $m_{\rm ex} \geq 4.5, 5.0, 6.1, 6.4$, and 7.1. First, the probabilities were computed

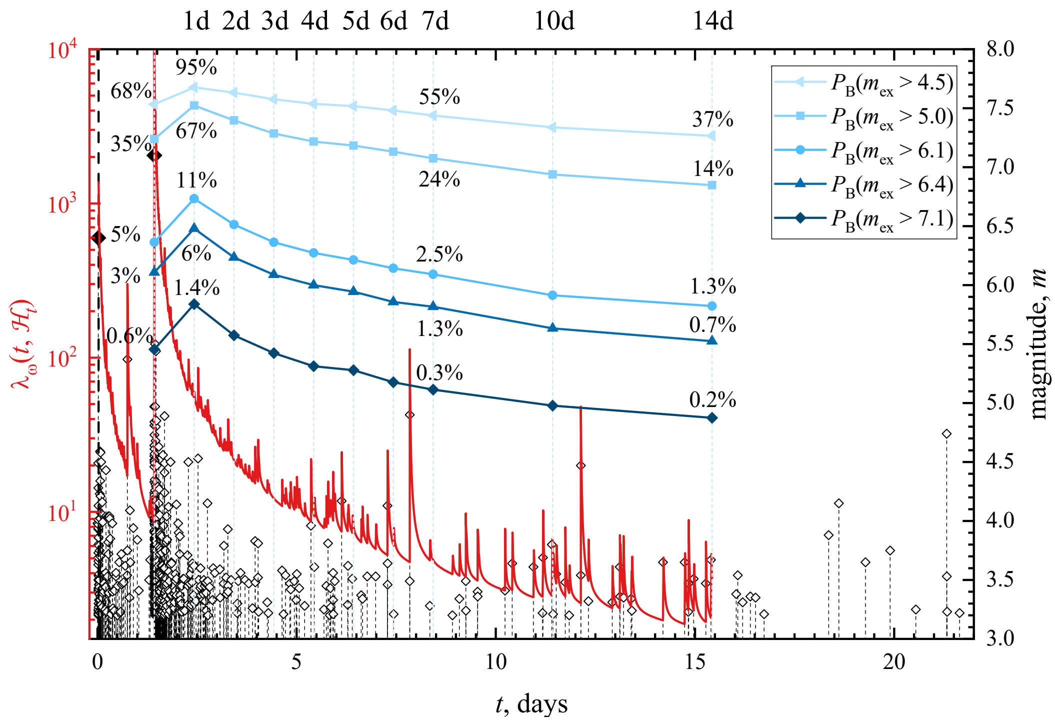

Figure 8. The probabilities for the largest expected earthquake to be above the magnitudes $m_{ex} \geq 4.5, 5.0, 6.1, 6.4, 7.1$ and during the progressively increasing time intervals since 2019/07/04 (17:02:55 UTC). The probabilities are estimated using the BPD combined with the ETAS model for the earthquake rate during the forecasting time interval $\Delta T = 7$ days and plotted in a logarithmic scale. The earthquake magnitudes of the 2019 Ridgecrest sequence are plotted as open diamonds for all events above magnitude $m \geq 3.2$. The fit of the ETAS model is shown as a solid curve.

using only the foreshock sequence right before the occurrence of the M7.1 mainshock with $T_e = 1.4284$ days. After that, the probabilities were recomputed for each subsequent day after the M7.1 mainshock by incorporating the information from the newly occurred aftershocks. For reference, the fit of the ETAS model is also shown as a red curve using the following estimated model parameters $\{\beta, \mu, K, c, p, \alpha\} = \{2.39, 0.05, 3.47, 0.01, 1.35, 2.05\}$ during the training time interval $[T_s, T_e] = [0.03, 15.4284]$ days. The forecast evolution during 330 days after the occurrence of the M7.1 mainshock is given in Figure S12. It also illustrates the computed probabilities before the occurrence of the M5.5 event, which occurred on June 4, 2020.

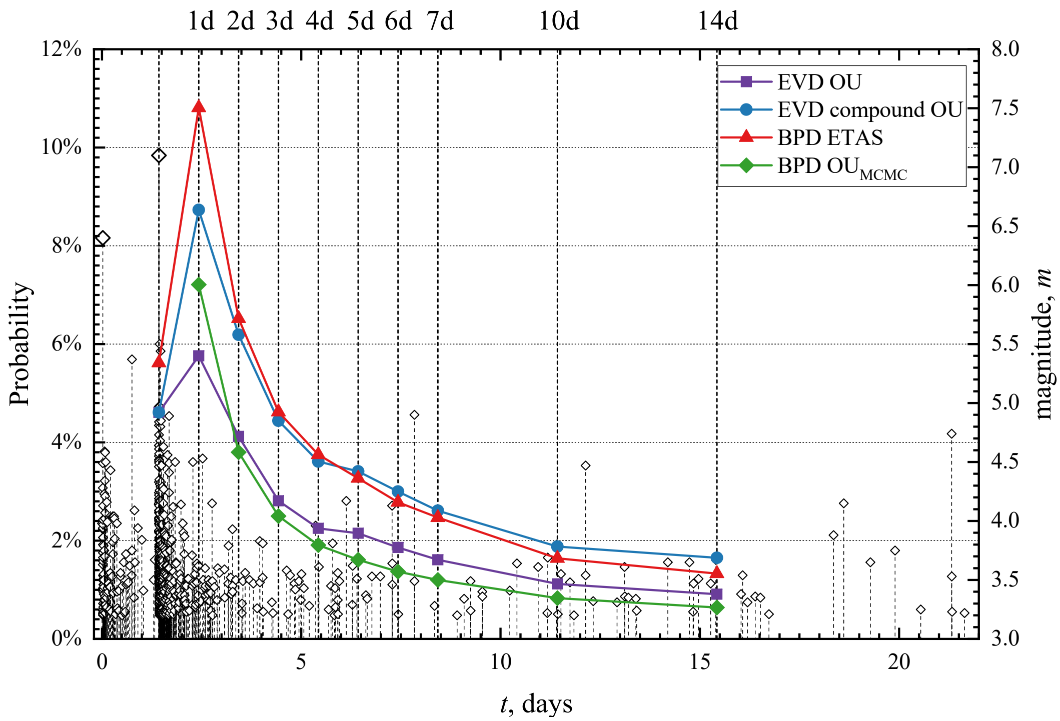

Figure 9. The comparison of the computed probabilities for the largest expected aftershock to be above magnitude $m_{\text{ex}} \geq 6.1$ during the progressively increasing time intervals since 2019/07/04 (17:02:55 UTC) for the fixed forecasting time interval $\Delta T = 7$ days. The four models were considered: the EVD with the OU law (solid squares), the EVD with the compound OU formula (solid circles), the BPD with the ETAS model (solid triangles), and the BPD with the OU law (solid diamonds).

Finally, Figure 9 provides a comparison of the results for the computation of the probabilities to have the expected largest aftershock to be greater than $m_{\text{ex}} \geq 6.1$ after progressively increasing times T_e during the evolution of the sequence by using several methods examined in this work. The forecasting time interval was set to $\Delta T = 7$ days. Specifically, the EVD with the OU law, Eqs. (8) and (9), was used and the estimated probabilities are plotted as solid squares. Next, the compound OU law (10) was used in the EVD computation and the results are plotted as solid circles. The computed probabilities from the BPD (11) with the ETAS model (6) as the earthquake rate are plotted as solid triangles. Finally, the probabilities were computed from the BPD with the earthquake rate modelled using the standard OU law (4) and are plotted as solid diamonds.

4 Forecast Validation

The extreme value distribution, Eq. (8), and the Bayesian predictive distribution, Eq. (11), allow to compute the probability of having the expected largest event during the forecasting time interval ΔT. This computation critically depends on the proper simulation of the earthquake rate and the frequency-magnitude distribution of earthquakes during ΔT. Therefore, it is important to perform specific statistical tests to validate retrospectively as to how the models, that are used to describe those aspects of seismicity, accurately reproduce the observed earthquakes during the forecasting time intervals. One such test has been developed for the CSEP testing framework and is known as the N-test (Kagan & Jackson, 1995; Schorlemmer et al., 2007; Zechar et al., 2010). This test is used to quantify as to how accurately a given stochastic process reproduces the observed number of earthquakes above a certain magnitude during the forecasting time interval.

The following implementation of the N-test is considered in this work. It is assumed that N_{obs} earthquakes above magnitude m_0 occurred during a given forecasting time interval $[T_e, T_e + \Delta T]$. The posterior distribution of the parameters of a given stochastic point process model is sampled by the MCMC method N_{sim} times using the information of the earthquakes that occurred during the training time interval $[T_s, T_e]$. The MCMC sets of the model parameters are used to model forward in time a given point process during the forecasting time interval ΔT. The synthetic simulations produce the distribution of the number of the forecasted events at the end of the interval ΔT corresponding to each MCMC set of model parameters. The N-test statistically assesses whether the observed number of earthquakes N_{obs} is consistent with the forecast. The two quantile scores are computed (Zechar et al., 2010):

$$\delta_1 = 1 - P\left(N_{\mathrm{obs}} - 1 | N_{\mathrm{fore}}\right) , \tag{12}$$

$$\delta_2 = P\left(N_{\mathrm{obs}} | N_{\mathrm{fore}}\right) , \tag{13}$$

where N_{fore} is the average number of forecasted events above magnitude m_0 at the end of the forecasted time interval $T_e{+}\Delta T$. $P(x|\lambda)$ is the cumulative Poisson distribution with the expectation λ. As a result, δ_1 gives the probability of observing at least N_{obs} events and δ_2 gives the probability of observing at most N_{obs} events. The forecast underpredicts the observations if δ_1 is very small and the forecast overpredicts the observation if δ_2 is very small. Therefore, one can consider a one-sided test with an effective significance level α_{eff}. If the computed probabilities δ_1 and δ_2 are smaller than α_{eff} then the forecast can be rejected.

The second test, which is known as M-test, has been suggested to check whether the distribution of the forecasted magnitudes is consistent with the observed magnitudes (Schorlemmer et al., 2007; Zechar et al., 2010). The M-test is performed by computing a quantile score κ. The values of κ below a significance level α_{eff} signify that the distribution of forecasted earthquake magnitudes is inconsistent with observations. The details of computing the κ score can be found in Zechar et al. (2010).

Two more tests have been introduced to compare the performance of different forecasting models. These are known as R-test and T-test (Schorlemmer et al., 2007; Rhoades et al., 2011). The R-test is performed by computing the log-likelihood ratio for two models under consideration. The joint log-likelihood for given earthquake observations during the forecasting time interval can be written as follows:

$$L(\mathbf{M}|\mathbf{\Lambda}) = \log\left[\Pr(\mathbf{M}|\mathbf{\Lambda})\right] = \sum_{i\in\mathbf{B}} \left\{-\lambda(i) + m(i)\log[\lambda(i)] - \log[m(i)!]\right\}, \tag{14}$$

where $\mathbf{M} = \{m(i)|i \in \mathbf{B}\}$ is the set of the number of earthquakes $m(i)$ in each magnitude bin above a certain magnitude threshold. $\mathbf{\Lambda} = \{\lambda(i)|i \in \mathbf{B}\}$ is the earthquake forecast produced by a given point process in each magnitude bin, where $\lambda(i)$ is the number of earthquakes forecasted in bin i and the magnitude binning coincides with the binning of the earthquake catalog. In the definition of the joint log-likelihood, Eq. (14), it is assumed that the number of earthquakes in a forecast bin follows a Poisson distribution: $\Pr(m|\lambda) = \frac{\lambda^m}{m!}\exp(-\lambda)$. To compare two models, $\mathbf{\Lambda}^1$ and $\mathbf{\Lambda}^2$, that forecast the same sequence of events one can compute the log-likelihood ratio: $R^{21} = L(\mathbf{M}|\mathbf{\Lambda}^2) - L(\mathbf{M}|\mathbf{\Lambda}^1)$.

In applying the R-test, one of the two models is assumed to be correct and is used to simulate the ensemble of synthetic earthquake events and compute the log-likelihood ratios for each synthetic record by using both models. These ratios are compared with the log-likelihood ratio computed for the observed earthquake sequence during the forecasting interval. The properly normalized fraction of the simulated ratios that are less than the observed ratio gives the quantile score α (Schorlemmer et al., 2007). The values of α, that are larger than a certain significance level, support the model that was assumed to be correct. This test is symmetric with respect to both models and can result in the situations when both models reject each other (Rhoades et al., 2011). To overcome this difficulty, a so called T-test was introduced along with the sample information gain per earthquake (Rhoades et al., 2011). The sample information gain per earthquake of the model $\mathbf{\Lambda}^2$ over the model $\mathbf{\Lambda}^1$ is defined as $I_N(\mathbf{\Lambda}^2, \mathbf{\Lambda}^1) = R^{21}/N_{\text{obs}}$, where N_{obs} is the number of observed earthquakes during the forecasting time interval ΔT. The T-test checks whether the sample information gain is statistically different from zero that indicates a significant difference between the two models (Rhoades et al., 2011).

One important difference in performing the above tests is implemented in this work. To account for the stochastic variability of the model parameters and the uncertainty associated with the prior information on the model parameters, the MCMC sampling of the posterior distribution of the model parameters is performed to produce a chain of model parameters that are used when simulating the models forward in time during the forecasting time interval.

The N-, M-, R-, and T-tests check the consistency of the underlying earthquake rate and frequency-magnitude distribution models. To test the consistency of the Bayesian predictive distribution, Eq. (11), with the observed largest earthquakes during the forecasting time interval $[T_e,\, T_e + \Delta T]$, one can evaluate the posterior predictive p-value (Gelman et al., 2013, p.146). The Bayesian p_{B}-value gives the probability that the largest simulated earthquakes can be more extreme than the observed largest earthquake during the forecasting time interval. It is defined as follows:

$$p_{\text{B}} = \Pr\left[T(\hat{y}, \theta, \omega) \geq T(y, \theta, \omega) | y\right] \,, \tag{15}$$

where $T(y, \theta, \omega)$ is a *test quantity* computed for an observed variable y and simulated variable $\hat{y}$. The test quantity $T(y, \theta, \omega)$ characterizes data y with given model parameters θ and ω. It is used for model checking in Bayesian analysis similar to a test statistic in classical testing. One possible choice for the test quantity is: $T(y, \theta, \omega) = \max(y)$. In practice, the Bayesian p_{B}-value can be computed from the MCMC chain of the model parameters θ and ω. For each set of the model parameters, the stochastic forecasting model is simulated forward in time and the largest event is extracted. This will allow to compute $T(\hat{y}, \theta, \omega) = \max(\hat{y})$. The realized test quantity $T(y, \theta, \omega) = \max(y)$ is simply the value of the largest observed earthquake during the forecasting time interval. Therefore, the estimated p_{B}-value is the proportion of the test quantities for the simulated maximum events that are larger than the observed largest event:

$$p_{\text{B}} = \frac{|\{T(\hat{y}, \theta_i, \omega_i) \geq T(y) | i = 1, ..., N_{\text{sim}}\}|}{N_{\text{sim}}} \,, \tag{16}$$

where N_{sim} is the total number of simulated sequences from the MCMC chain and $|x|$ gives the size of the set x.

4.1 Application to the 2019 Ridgecrest sequence

The three point process models (OU, compound OU, and ETAS) were examined to see whether they were consistent with the observed seismicity during the forecasting time intervals $[T_e, T_e{+}\Delta T]$. For this, N- and M-tests were performed. Figure 10a shows the observed number of earthquakes above magnitude $m \geq 3.2$ (as solid black diamonds) during a fixed forecasting time interval $\Delta T = 7$ days and varying training time interval $[T_s, T_e]$. The numbers are plotted at the end of the forecasting time interval with the training interval ending after 1, 2, 3, 4, 5, 6, 7, 10, 14, 30 days after the M7.1 mainshock (the corresponding $T_e\ =\ 2.4284, 3.4284, ..., 22.4284, 31.4284$). For example, the first symbol at $T_e + \Delta T = 9.4284$ days gives 89 earthquakes above magnitude 3.2 that occurred during 7 days starting after 1 day ($T_e\ =\ 2.4284$) after the M7.1 mainshock. It also shows the average forecasted numbers of earthquakes with the corresponding 95% bands (plotted as shaded regions) simulated by the three models. Each model was simulated $N_{\mathrm{sim}}\ =\ 100,000$ times forward in time during $\Delta T\ =\ 7$ days and for the varying ends of the training time interval T_e. For each model simulation, the parameters were chosen from the MCMC chain obtained by sampling the posterior distribution of the model parameters. This allowed to incorporate the variability of the model parameters into the forecasted numbers. Similarly, Figure 10b illustrates the observed and forecasted number of earthquakes when the end of the training time interval was held fixed at $T_e = 3.4284$ days (2 days after the M7.1 mainshock) and the forecasting time interval varied $\Delta T =$ 1, 2, 5, 7, 10, 14 days. For the compound OU and ETAS models the preceding foreshock sequence was used. For the OU model only the aftershocks of the M7.1 mainshock were used.

To analyze to what extent the considered models underpredicted or overpredicted the observed sequence of earthquakes, the N-test was performed. The quantile scores computed during the N-test corresponding to the forecasting of the number of earthquakes are illustrated in Figure 11ab. Two threshold quantiles are plotted at 0.025 and 0.05 levels. δ_1 and δ_2 scores, Equations (12) and (13), were computed and plotted for the three models for the same forecasting time intervals of duration $\Delta T = 7$ days as used in Figure 10a. In addition, the results of the M-test for the three models and for the same fore-

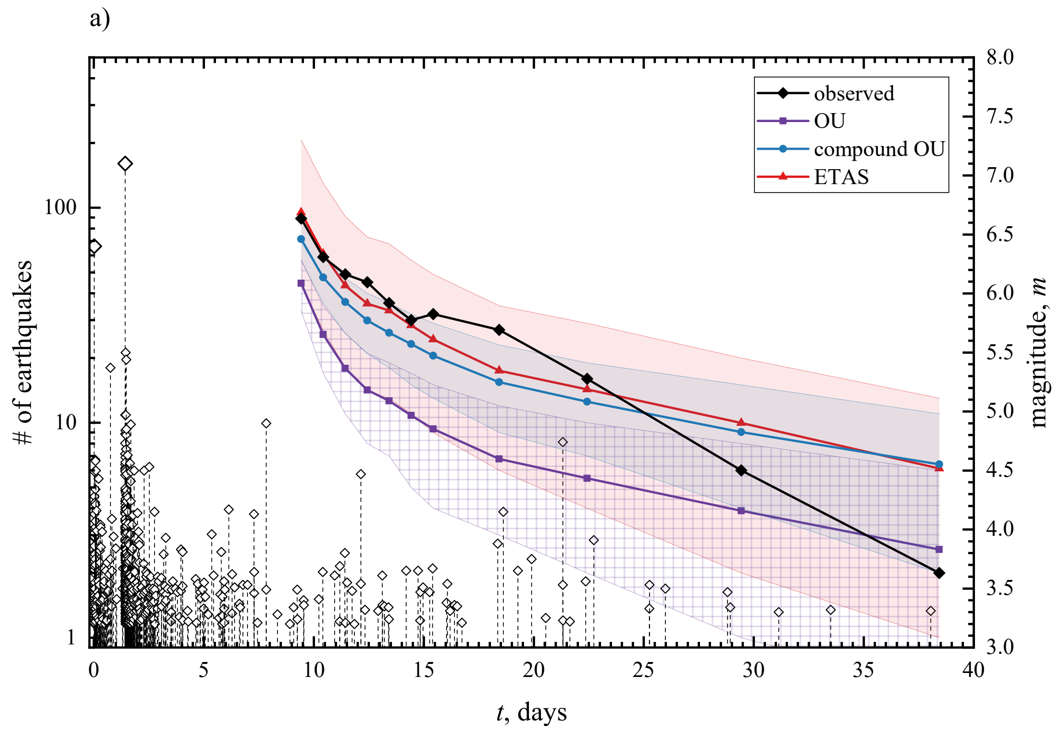

Figure 10. The observed and forecasted numbers of earthquakes starting after one day of aftershocks post M7.1 mainshock and during specified forecasting and training time intervals by using the three rate models: Omori-Utsu (OU), compound OU, and ETAS. a) The forecasting time interval $\Delta T = 7$ days is fixed while the end of the training time interval T_e is progressively increasing as $T_e = 2.428$, 3.428, ..., 22.428, 31.428 days. The symbols indicate the number of the observed (black solid diamonds) and the mean number of forecasted earthquakes during $\Delta T = 7$ days computed at times $T_e + \Delta T$. b) The end of the training time interval is fixed at $T_e = 3.428$ days while the forecasting time interval is increasing as $\Delta T = 1$, 2, 5, 7, 10, 14. The shaded bands correspond to 95% confidence intervals.

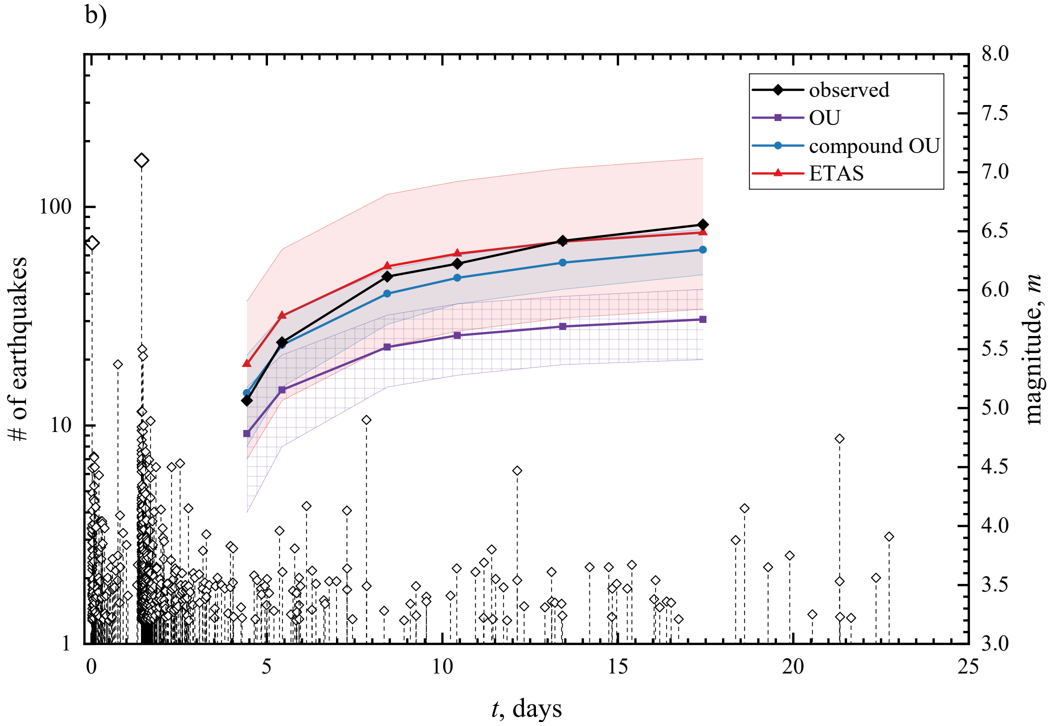

Figure 10. Continued.

casting time intervals are plotted in Figure 11c, where the quantile score κ characterizes the consistency of the forecasted earthquake magnitudes compared to the observed ones in each forecasting time interval. The quantile scores in a case of the varying forecasting time interval $\Delta T = 1$, 2, 5, 7, 10, 14 days and fixed training time interval $T_e = 3.4284$ days are given in Figure S13.

The models were also compared among each other by applying the R- and T-tests. Two pairs of the models were considered, i.e. the forecasts produced by the ETAS model versus the model with the OU law and the ETAS model versus the model with the compound OU law. The results of the quantile score α for the R-test are plotted in Figure 12. The scores α were computed at the end of each forecasting time interval of duration ΔT as in Figure 10a. The corresponding sample information gain $I_N(\mathbf{\Lambda}^2, \mathbf{\Lambda}^1)$ for each pair of the models is given in Figure 13. The quantile score α and the information gain per earthquake in a case of the varying forecasting time interval $\Delta T = 1$, 2, 5, 7, 10, 14 days and fixed training time interval $T_e = 3.4284$ days are given in Figures S14 and S15. In both pairs of models, it was assumed that the ETAS model (with the forecast $\mathbf{\Lambda}^2$) is the

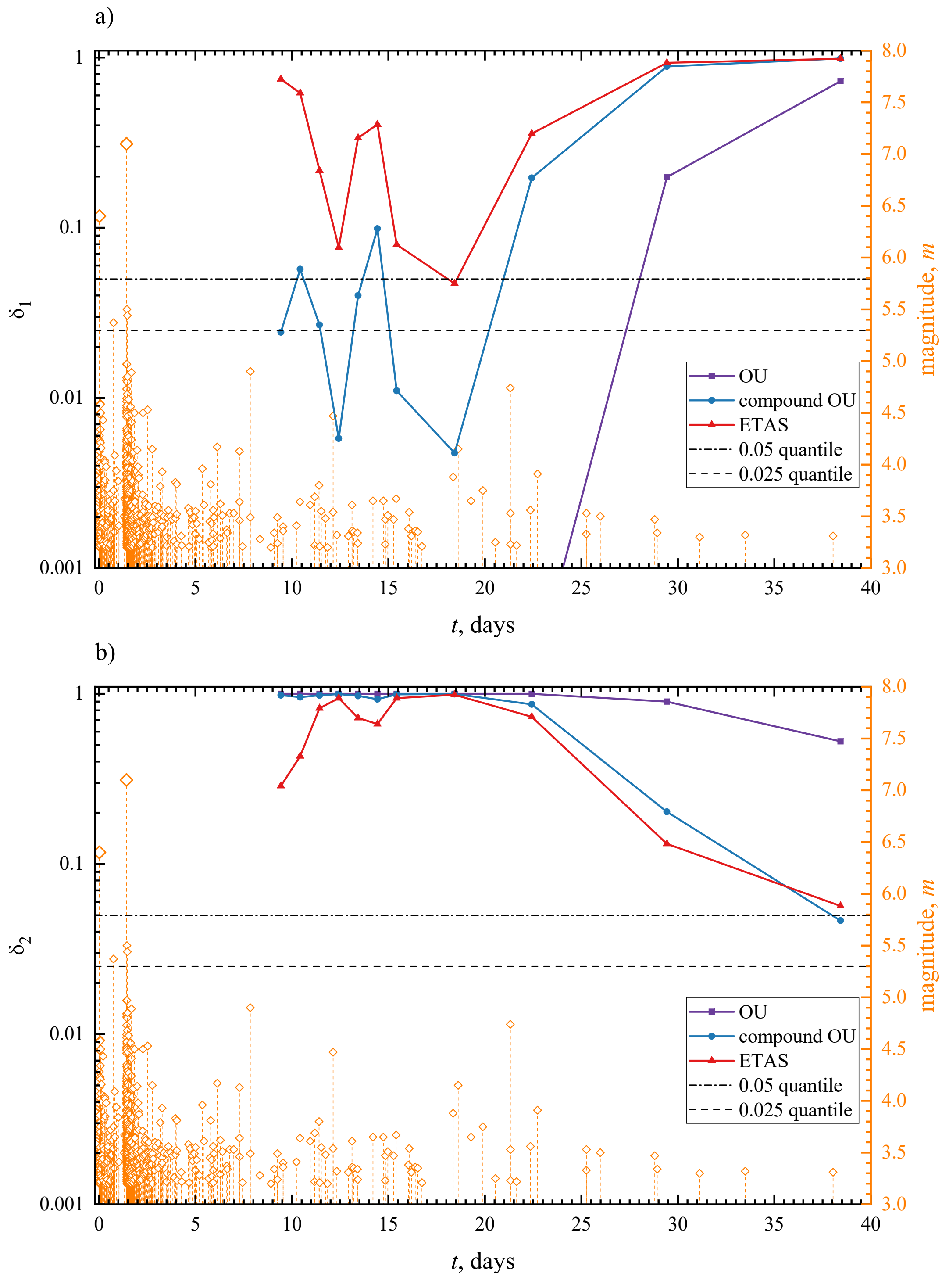

Figure 11. Plot of the quantile scores a) δ_1 (N-test), b) δ_2 (N-test), and c) κ (M-test) for the performance of the aftershock forecasts based on the three point process models. The scores are computed at the end of each forecasting time interval of fixed duration $\Delta T = 7$ days and varying training time intervals $[T_s, T_e]$ as in Figure 10.

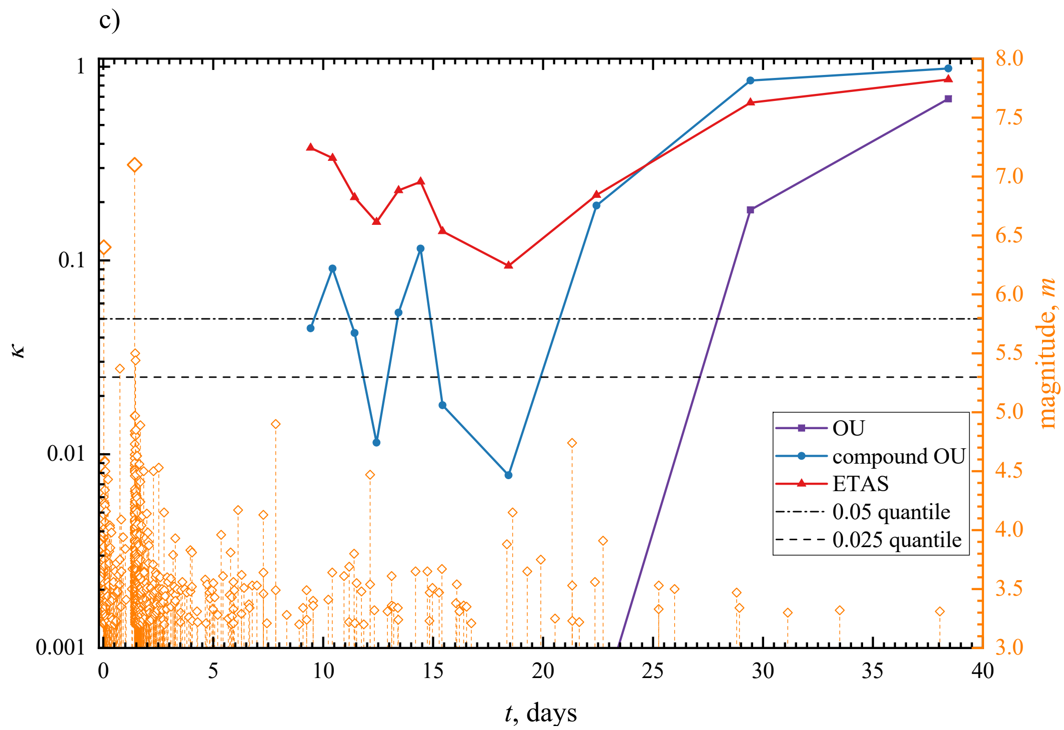

Figure 11. Continued.

correct model to simulate the synthetic sequences of events during the forecasting time intervals.

Finally, the Bayesian p_B-value, Eq. (16), was computed for the three models. This is plotted in Figure 14 for the varying training time intervals. Figure S16 illustrates the dependency of the p_B-value on the varying forecasting time interval as in Figure S14.

5 Discussion

The 2019 Ridgecrest earthquake sequence occurred in a complex network of fault structures. It generated a prominent foreshock sequence that culminated in the occurrence of the M7.1 mainshock, which was followed by a productive aftershock sequence. This complexity of the sequence was partially reflected in the frequency-magnitude statistics of foreshocks and aftershocks. It also manifested in the clustering of earthquakes in time and in space. The complex pattern of multi-segmented ruptures of the two strongest events in the sequence contributed to the assumed stress transfer pattern, which affected the distribution of subsequent triggered aftershocks.

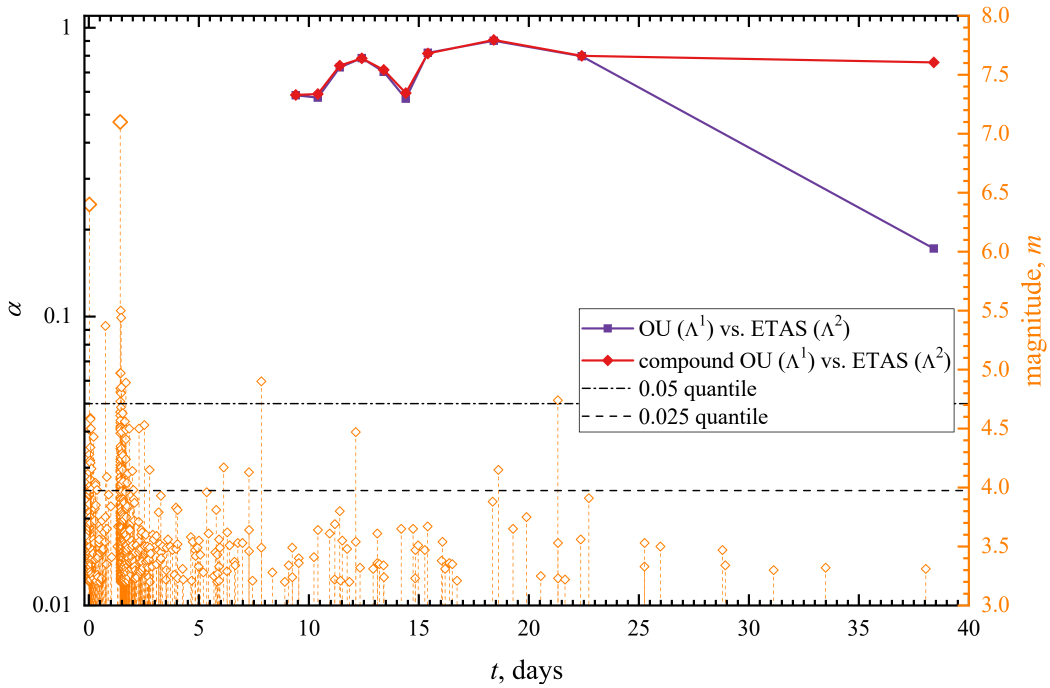

Figure 12. Plot of the quantile score α (R-test) for the comparative test of the ETAS model versus the forecast based on the OU model and on the compound OU model. The scores are computed at the end of each forecasting time interval as in Figure 11.

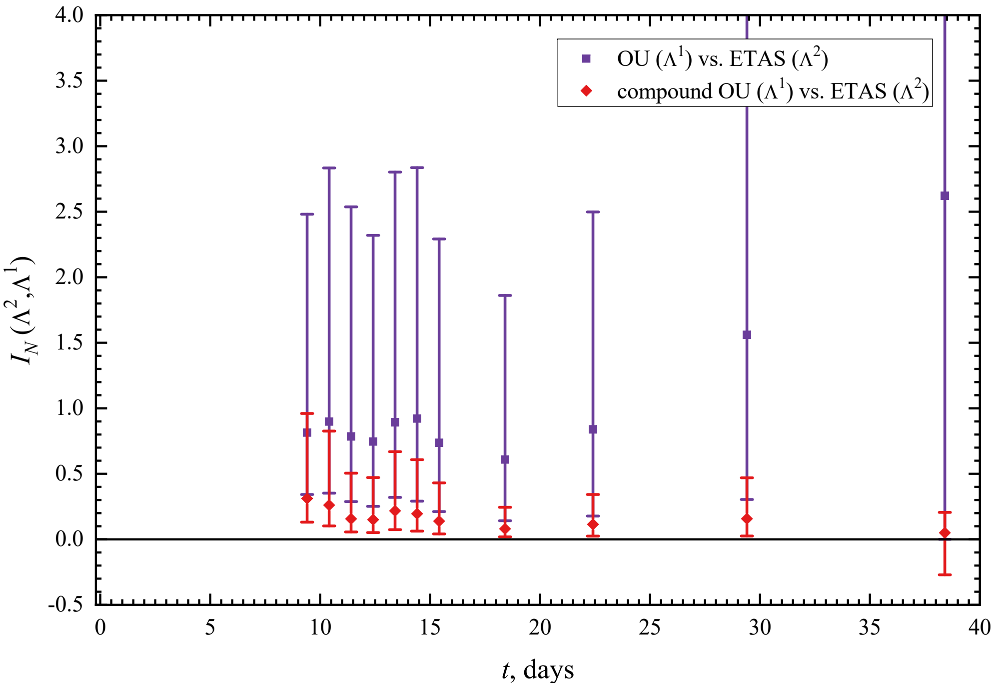

Figure 13. The sample information gain for the pairs of the models. The solid squares correspond to the comparison of the forecasts based on the ETAS model versus the forecasts based on the OU model. The solid diamonds correspond to the comparison of the forecasts based on the ETAS model versus the forecast based on the compound OU model. The 95% confidence intervals are given.

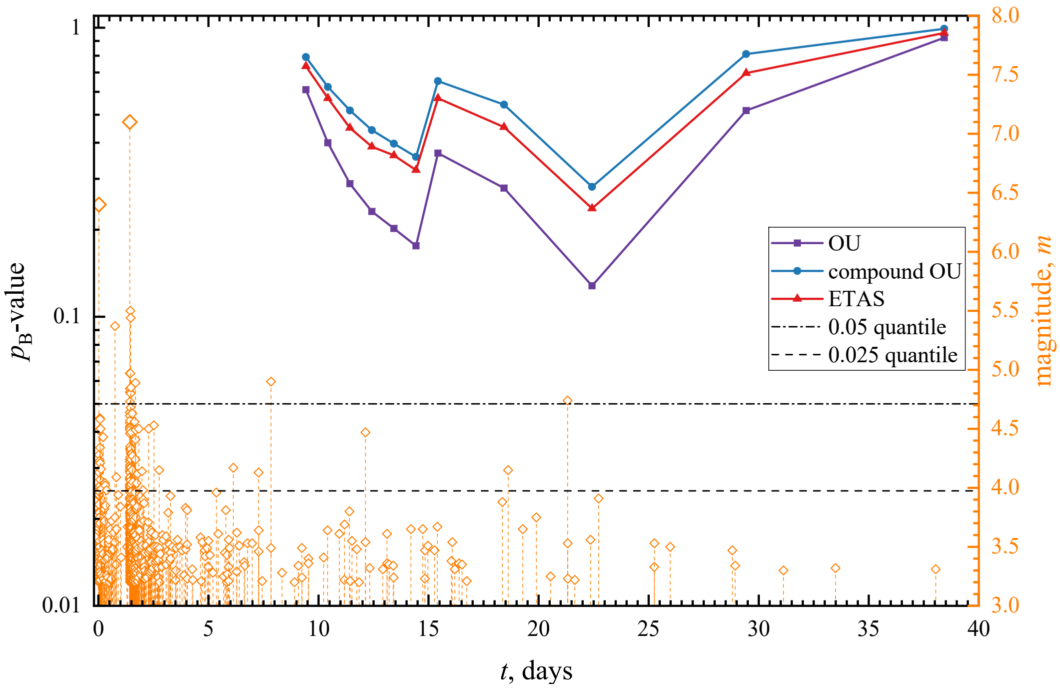

Figure 14. Plot of the Bayesian predictive distribution p_{B}-value for the three models. The p_{B}-values are computed at the end of each forecasting time interval as in Figure 11.

One of the main objectives of this work was to provide a framework to compute the probabilities for the occurrence of the largest expected aftershocks during different stages of the evolution of this sequence by incorporating the preceding seismicity. This was accomplished through two main approaches. The first one was based on the assumption that the occurrence of earthquakes could be modelled as a non-homogenous Poisson process with a specified parametric model for the earthquake rate and the frequency-magnitude distribution. Specifically, one can use the OU law (4) or the compound OU law (5) and the exponential distribution for the earthquake magnitudes, Eq. (2). Then, the probabilities can be estimated from the EVD (8) for a specific forecasting time interval ΔT by using the point estimates of the model parameters. The second approach employed the computation of the BPD (11), which allowed to incorporate the uncertainties of the model parameters into the computation of the corresponding probabilities. This approach also requires to provide certain *a priori* knowledge on the model parameters specified through the prior distributions.

The comparison of these two approaches with the combination of the three models for the earthquake rate and either including or excluding the foreshocks is illustrated in Figure 7. The results clearly illustrate that the inclusion of the foreshocks along with the earthquake rate models that favour earthquake clustering produces higher probabilities for the occurrence of the largest expected earthquakes during the specified forecasting period of $\Delta T = 7$ days.

It is interesting to note, the 2019 Ridgecrest earthquake sequence bears a striking similarity to the 2016 Kumamoto, Japan, earthquake sequence. Both sequences had a pronounced foreshock sequence which was triggered by the strong foreshocks of similar magnitudes (M6.4 vs. M6.5) and duration. They occurred on the different fault segments than the mainshock fault rupture. The b-values of the GR relation and p values of the OU law were also smaller than the values for the aftershocks generated by the mainshocks. The mainshock magnitudes were also similar (M7.1 vs. M7.3) and had the strike-slip mechanisms. It is difficult to pin point the common stress conditions and state of faults that lead to the occurrence of both sequences but some clues may be inferred from the seismicity patterns that preceded and followed both events and can be related to the changes in the stress field (Nanjo et al., 2019; Nanjo, 2020).

To validate the three stochastic models, several statistical tests (N-, M-, R-, and T-tests) were applied retrospectively for several combinations of the training and forecasting time intervals. The results of the N-test indicate that the OU model underestimated the observed number of earthquakes for most of the forecasting time intervals. The compound OU model performed better especially in the early stages of the evolution of the sequence. The ETAS model approximated the observed number of earthquakes during the all considered forecasting time intervals, however, the ETAS model also had wider 95% spread in the number of forecasted earthquakes (Figure 10). This is the consequence of the branching nature of the ETAS process and the deviation of the distribution of the number of events from the Poisson distribution. The ETAS model was also consistent in reproducing the distribution of the magnitudes in each bin that is illustrated in Figure 11c through the κ quantile score of the M-test.

The comparative analysis of the ETAS model versus the OU and the compound OU models also confirmed that the forecast based on the ETAS model outperformed the forecasts based on the other two models. This is illustrated in Figure 12, where the quantile score α from the R-test is plotted at the end of each forecasting time interval. The values of the score above the threshold level 0.025 indicate that the ETAS model outperformed the other two models. The similar conclusion is drawn from the plot (Figure 13) of the sample information gain $I_N(\mathbf{\Lambda}^2, \mathbf{\Lambda}^1)$. The results of the T-test confirmed that the ETAS model provided a statistically significant information gain with respect to the models based on the OU or compound OU rates except for the last forecasting interval ending at 38.4284 days, where the ETAS model and the model based on the compound OU rate performed similarly. For the last forecasting time interval ending at $T_e + \Delta T = 38.4284$ days, there were only three events above magnitude $m \geq 3.2$. The compound OU model produced relatively close results when computing the probabilities for the occurrence of the largest expected earthquakes (Figure 9).

One limitation of the above tests (M-, R-, T-) based on the computing of the joint log-likelihoods, Eq. (14), is that they assume that the distribution of the number of earthquakes in the forecasting time interval is Poisson. This is true for the both point process models based on the OU law. However, the ETAS model deviates from the Poisson assumption. This was already demonstrated in Shcherbakov et al. (2019) when computing the Bayesian predictive distribution. Therefore, the application of these tests to the ETAS based models has to be considered approximate.

The above tests implemented in this work used the MCMC sampling of the posterior distribution of the model parameters. This allowed to incorporate the stochastic variability of the model parameters and the uncertainties associated with the prior information on the model parameters into the computation of the resulting probabilities and when performing the statistical tests. The consistency of the Bayesian predictive distribution was evaluated by estimating the Bayesian p_{B}-value, Eq. (16). The values of p_{B} within a reasonable range (say [0.05, 0.95]) indicate that a model is expected to reproduce a specific aspect of the data given by the test quantity $T(y)$. Whereas, the values close to 0 or 1 signify that this aspect of the data is not captured by the model. All the three models were consistent in reproducing the observed largest earthquakes in each forecasting time interval.

The analysis of the 2019 Ridgecrest earthquake sequence showed that the Bayesian predictive framework combined with the ETAS model outperformed more traditional approaches based on the Omori-Utsu type models when using the extreme value distribution to compute the probabilities for the occurrence of the largest events. The latter approach uses point estimates of the model parameters to compute the corresponding probabilities. However, large uncertainties associated with these model parameters can result in significant underestimation/overestimation of the probabilities for the largest expected events or the numbers of earthquakes above a certain magnitude during the forecasting time intervals. This is particularly evident for the Omori-Utsu law, where the productivity of the process is controlled by the K_o parameter, which is typically estimated with large uncertainties (Marsan & Helmstetter, 2017; Shebalin et al., 2020). On the other hand, the Bayesian framework fully incorporates these model uncertainties into the computation of the probabilities. It also allows to account for the correlations among the model parameters. In addition, the Bayesian approach provides a flexible way of separating those uncertainties into epistemic and aleatory types (Kiureghian & Ditlevsen, 2009; Gerstenberger et al., 2020). It allows to control the epistemic uncertainties through the prior information of the model parameters and incorporates the aleatory variability of the stochastic process through the earthquake rate models and the frequency-magnitude distributions.

6 Conclusions

The 2019 Ridgecrest earthquake sequence was characterized by the complex clustering of seismicity with earthquakes occurring on a distributed fault network. It also presented a good opportunity to analyze the sequence retrospectively in order to test several statistical approaches to study the sequence in temporal and magnitude domains and to forecast the occurrence of the largest expected aftershocks during the evolution of the sequence.

Two approaches were used to compute the probabilities of having the largest expected earthquakes to be above certain magnitudes after specified time intervals and during the fixed forecasting time interval $\Delta T = 7$ days. For the first approach, the EVD (8) with the OU law (4) or the compound OU formula (5) was used. In the second approach, the Bayesian predictive distribution, Eq. (11), combined with the OU law or the ETAS model (6) was used. The comparison of these approaches are illustrated in Figure 9.

Applying these two approaches to the 2019 Ridgecrest earthquake sequence revealed that the incorporation of the foreshock sequence for the subsequent computation of the probabilities to have the largest expected aftershocks above a certain magnitude was important. This was also relevant to the choice of the model to approximate the earthquake rate. Specifically, the compound OU law (5) and the ETAS model (6) provided a better approximation for the earthquake rate than the OU law (4) applied separately to the foreshock and aftershock sequences during the forecasting time intervals. These conclusions have been verified by several statistical tests. In addition, a new test based on the Bayesian p_{B}-value was implemented and applied to check the consistency of the Bayesian predictive distribution. Overall, the ETAS model passed the tests most of the time and was successful in reproducing the observed number of earthquakes and the distribution of magnitudes. As a result, the computed probabilities using the Bayesian predictive distribution (Figure 8) for the largest expected earthquake during the evolution of the 2019 Ridgecrest sequence can be considered accurate.

Data and Resources

The Southern California Seismic Network database, SCSN (2020), `https://service.scedc.caltech.edu/eq-catalogs/date\_mag\_loc.php`, was used to download the seismic catalog (last accessed on December 1, 2020).

U.S. Geological Survey and California Geological Survey quaternary fault and fold database for the United States , USGS (2006), was downloaded from the USGS web site: `https://earthquake.usgs.gov/hazards/qfaults/` (last accessed on June 1, 2020).

The data analysis was performed using computer scripts written in Matlab and can be requested from the author.

The Supporting Information for this article includes Tables S1-S3 with the parameters of the Gamma distribution, which was used as a prior distribution for the parameters of the three models considered in the work. It also includes plots illustrating the fit of the compound OU (Figure S1) and the ETAS (Figure S2) models. The MCMC sampling of the model parameters for the OU (Figures S4-S5), the compound OU (Figures S6-8), the ETAS (Figures S9-S11) models are provided for one specific training and forecasting time intervals. The forecast evolution during 330 days after the occurrence of the M7.1 mainshock is given in Figure S12. The additional quantile scores of the plots are given in Figures S13-S16.

Acknowledgments

The constructive comments by two anonymous reviewers helped to improve the manuscript. This work has been supported by the NSERC Discovery grant.

References

Barnhart, W. D., Hayes, G. P., & Gold, R. D. (2019). The July 2019 Ridgecrest, California, earthquake sequence: Kinematics of slip and stressing in cross-fault ruptures. *Geophys. Res. Lett.*, *46*, 11859-11867. doi: 10.1029/2019gl084741

Båth, M. (1965). Lateral inhomogeneities of the upper mantle. *Tectonophysics*, *2*, 483-514.

Bender, B. (1983). Maximum likelihood estimation of b values for magnitude grouped data. *Bull. Seismol. Soc. Am.*, *73*(3), 831-851.

Campbell, K. W. (1982). Bayesian analysis of extreme earthquake occurrences. Part I. Probabilistic hazard model. *Bull. Seismol. Soc. Am.*, *72*(5), 1689-1705.

Cattania, C., Werner, M. J., Marzocchi, W., Hainzl, S., Rhoades, D., Gerstenberger, M., ... Jordan, T. H. (2018). The forecasting skill of physics-based seismicity models during the 2010-2012 Canterbury, New Zealand, earthquake sequence. *Seismol. Res. Lett.*, *89*(4), 1238-1250. doi: 10.1785/0220180033

Coles, S. (2001). *An Introduction to Statistical Modeling of Extreme Values.* London: Springer.

Console, R., Lombardi, A. M., Murru, M., & Rhoades, D. (2003). Båth's law and the self-similarity of earthquakes. *J. Geophys. Res.*, *108*(B2), 2128. doi: 10.1029/2001JB001651

Daley, D. J., & Vere-Jones, D. (2003). *An Introduction to the Theory of Point Processes* (2nd ed., Vol. 1). New York: Springer.

Ebrahimian, H., & Jalayer, F. (2017). Robust seismicity forecasting based on Bayesian parameter estimation for epidemiological spatio-temporal aftershock clustering models. *Sci. Rep.*, *7*, 9803. doi: 10.1038/s41598-017-09962-z

Ebrahimian, H., Jalayer, F., Asprone, D., Lombardi, A. M., Marzocchi, W., Prota, A., & Manfredi, G. (2014). Adaptive daily forecasting of seismic aftershock hazard. *Bull. Seismol. Soc. Am.*, *104*(1), 145-161. doi: 10.1785/0120130040

Felzer, K. R., Abercrombie, R. E., & Ekström, G. (2004). A common origin for aftershocks, foreshocks, and multiplets. *Bull. Seismol. Soc. Am.*, *94*(1), 88-98.

doi: 10.1785/0120030069

Gelman, A., Carlin, J., Stern, H., Dunson, D., Vehtari, A., & Rubin, D. (2013). *Bayesian Data Analysis* (3rd ed.). Boca Raton: CRC Press.

Gerstenberger, M. C., Marzocchi, W., Allen, T., Pagani, M., Adams, J., Danciu, L., ... Petersen, M. D. (2020). Probabilistic seismic hazard analysis at regional and national scale: State of the art and future challenges. *Rev. Geophys.*, *58*(2), e2019RG000653. doi: 10.1029/2019rg000653

Gerstenberger, M. C., Wiemer, S., Jones, L. M., & Reasenberg, P. A. (2005). Real-time forecasts of tomorrow's earthquakes in California. *Nature*, *435*(7040), 328-331. doi: 10.1038/Nature03622

Gutenberg, B., & Richter, C. F. (1944). Frequency of earthquakes in California. *Bull. Seismol. Soc. Am.*, *4*, 185-188.

Hainzl, S. (2016a). Apparent triggering function of aftershocks resulting from rate-dependent incompleteness of earthquake catalogs. *J. Geophys. Res.*, *121*(9), 6499-6509. doi: 10.1002/2016jb013319

Hainzl, S. (2016b). Rate-dependent incompleteness of earthquake catalogs. *Seismol. Res. Lett.*, *87*(2), 337-344. doi: 10.1785/0220150211

Hardebeck, J. L. (2020). A stress-similarity triggering model for aftershocks of the M_w 6.4 and 7.1 Ridgecrest earthquakes. *Bull. Seismol. Soc. Am.*, *110*(4), 1716-1727. doi: 10.1785/0120200015

Hardebeck, J. L., Llenos, A. L., Michael, A. J., Page, M. T., & van der Elst, N. (2019). Updated California aftershock parameters. *Seismol. Res. Lett.*, *90*(1), 262-270. doi: 10.1785/0220180240

Harte, D. (2010). PtProcess: An R package for modelling marked point process indexed by time. *J. Stat. Softw.*, *35*(8), 1-32. doi: 10.18637/jss.v035.i08

Harte, D. (2017). Probability distribution of forecasts based on the ETAS model. *Geophys. J. Int.*, *210*(1), 90-104. doi: 10.1093/gji/ggx146

Helmstetter, A., Kagan, Y. Y., & Jackson, D. D. (2006). Comparison of short-term and time-independent earthquake forecast models for southern California. *Bull. Seismol. Soc. Am.*, *96*(1), 90-106. doi: 10.1785/0120050067

Holschneider, M., Narteau, C., Shebalin, P., Peng, Z., & Schorlemmer, D. (2012). Bayesian analysis of the modified Omori law. *J. Geophys. Res.*, *117*, B06317. doi: 10.1029/2011jb009054

Kagan, Y. Y. (2004). Short-term properties of earthquake catalogs and models of earthquake source. *Bull. Seismol. Soc. Am.*, *94*(4), 1207-1228.

Kagan, Y. Y., & Jackson, D. D. (1995). New seismic gap hypothesis: Five years after. *J. Geophys. Res.*, *100*(B3), 3943-3959. doi: 10.1029/94jb03014

Kiureghian, A. D., & Ditlevsen, O. (2009). Aleatory or epistemic? Does it matter? *Struct. Safety*, *31*(2), 105-112. doi: 10.1016/j.strusafe.2008.06.020

Liu, C. L., Lay, T., Brodsky, E. E., Dascher-Cousineau, K., & Xiong, X. (2019). Coseismic rupture process of the large 2019 Ridgecrest earthquakes from joint inversion of geodetic and seismological observations. *Geophys. Res. Lett.*, *46*, 11820-11829. doi: 10.1029/2019gl084949

Mancini, S., Segou, M., Werner, M. J., & Parsons, T. (2020). The predictive skills of elastic Coulomb rate-and-state aftershock forecasts during the 2019 Ridgecrest, California, earthquake sequence. *Bull. Seismol. Soc. Am.*, *110*(4), 1736-1751. doi: 10.1785/0120200028

Marsan, D., & Helmstetter, A. (2017). How variable is the number of triggered aftershocks? *J. Geophys. Res.*, *122*(7), 5544-5560. doi: 10.1002/2016jb013807

Michael, A. J., McBride, S. K., Hardebeck, J. L., Barall, M., Martinez, E., Page, M. T., … Wein, A. M. (2019). Statistical seismology and communication of the USGS operational aftershock forecasts for the 30 November 2018 MwÂ 7.1 Anchorage, Alaska, earthquake. *Seismol. Res. Lett.*, *91*(1), 153-173. doi: 10.1785/0220190196

Milner, K. R., Field, E. H., Savran, W. H., Page, M. T., & Jordan, T. H. (2020). Operational earthquake forecasting during the 2019 Ridgecrest, California, earthquake sequence with the UCERF3-ETAS model. *Seismol. Res. Lett.*, *91*(3), 1567-1578. doi: 10.1785/0220190294

Nanjo, K. Z. (2020). Were changes in stress state responsible for the 2019 Ridgecrest, California, earthquakes? *Nat. Commun.*, *11*(1). doi: 10.1038/s41467-020-16867-5

Nanjo, K. Z., Izutsu, J., Orihara, Y., Kamogawa, M., & Nagao, T. (2019). Changes in seismicity pattern due to the 2016 Kumamoto earthquakes identify a highly stressed area on the Hinagu fault zone. *Geophys. Res. Lett.*, *46*(16), 9489-9496. doi: 10.1029/2019gl083463

Nanjo, K. Z., Tsuruoka, H., Yokoi, S., Ogata, Y., Falcone, G., Hirata, N., …

Zhuang, J. (2012). Predictability study on the aftershock sequence following the 2011 Tohoku-Oki, Japan, earthquake: first results. *Geophys. J. Int.*, *191*(2), 653-658. doi: 10.1111/j.1365-246X.2012.05626.x

Ogata, Y. (1983). Estimation of the parameters in the modified Omori formula for aftershock frequencies by the maximum-likelihood procedure. *J. Phys. Earth*, *31*(2), 115-124. doi: 10.4294/jpe1952.31.115

Ogata, Y. (1988). Statistical-models for earthquake occurrences and residual analysis for point-processes. *J. Am. Stat. Assoc.*, *83*(401), 9-27.

Ogata, Y. (1999). Seismicity analysis through point-process modeling: A review. *Pure Appl. Geophys.*, *155*(2-4), 471-507. doi: 10.1007/s000240050275

Ogata, Y. (2017). Statistics of earthquake activity: Models and methods for earthquake predictability studies. *Annu. Rev. Earth Planet. Sci.*, *45*, 497-527. doi: 10.1146/annurev-earth-063016-015918

Ogata, Y., & Omi, T. (2020). Statistical monitoring and early forecasting of the earthquake sequence: Case studies after the 2019 M 6.4 Searles Valley earthquake, California. *Bull. Seismol. Soc. Am.*, *110*(4), 1781-1798. doi: 10.1785/0120200023

Omi, T., Ogata, Y., Hirata, Y., & Aihara, K. (2013). Forecasting large aftershocks within one day after the main shock. *Sci. Rep.*, *3*, 2218. doi: 10.1038/srep02218

Omi, T., Ogata, Y., Hirata, Y., & Aihara, K. (2014). Estimating the ETAS model from an early aftershock sequence. *Geophys. Res. Lett.*, *41*(3), 850-857. doi: 10.1002/2013gl058958

Omi, T., Ogata, Y., Shiomi, K., Enescu, B., Sawazaki, K., & Aihara, K. (2016). Automatic aftershock forecasting: A test using real-time seismicity data in Japan. *Bull. Seismol. Soc. Am.*, *106*(6), 2450-2458. doi: 10.1785/0120160100

Omi, T., Ogata, Y., Shiomi, K., Enescu, B., Sawazaki, K., & Aihara, K. (2019). Implementation of a reai-time system for automatic aftershock forecasting in Japan. *Seismol. Res. Lett.*, *90*, 242-250. doi: 10.1785/0220180213

Omori, F. (1894). On after-shocks of earthquakes. *J. Coll. Sci. Imp. Univ. Tokyo*, *7*, 113-200.

Page, M. T., van der Elst, N., Hardebeck, J., Felzer, K., & Michael, A. J. (2016). Three ingredients for improved global aftershock forecasts: Tectonic region, time-dependent catalog incompleteness, and intersequence variability. *Bull. Seismol. Soc. Am.*, *106*(5), 2290-2301. doi: 10.1785/0120160073

Peng, Z. G., Vidale, J. E., & Houston, H. (2006). Anomalous early aftershock decay rate of the 2004 Mw 6.0 Parkfield, California, earthquake. *Geophys. Res. Lett.*, *33*(17), L17307. doi: 10.1029/2006GL026744

Reasenberg, P. A., & Jones, L. M. (1989). Earthquake hazard after a mainshock in California. *Science*, *243*(4895), 1173-1176. doi: 10.1126/science.243.4895.1173

Renard, B., Sun, X., & Lang, M. (2013). Bayesian methods for non-stationary extreme value analysis. In A. AghaKouchak, D. Easterling, K. Hsu, S. Schubert, & S. Sorooshian (Eds.), *Extremes in a Changing Climate: Detection, Analysis and Uncertainty* (p. 39-95). Dordrecht: Springer.

Rhoades, D. A., Christophersen, A., Gerstenberger, M. C., Liukis, M., Silva, F., Marzocchi, W., ... Jordan, T. H. (2018). Highlights from the first ten years of the New Zealand earthquake forecast testing center. *Seismol. Res. Lett.*, *89*(4), 1229-1237. doi: 10.1785/0220180032

Rhoades, D. A., Liukis, M., Christophersen, A., & Gerstenberger, M. C. (2016). Retrospective tests of hybrid operational earthquake forecasting models for Canterbury. *Geophys. J. Int.*, *204*(1), 440-456. doi: 10.1093/gji/ggv447

Rhoades, D. A., Schorlemmer, D., Gerstenberger, M. C., Christophersen, A., Zechar, J. D., & Imoto, M. (2011). Efficient testing of earthquake forecasting models. *Acta Geophys.*, *59*(4), 728-747. doi: 10.2478/s11600-011-0013-5

Ross, Z. E., Idini, B., Jia, Z., Stephenson, O. L., Zhong, M. Y., Wang, X., ... Jung, J. (2019). Hierarchical interlocked orthogonal faulting in the 2019 Ridgecrest earthquake sequence. *Science*, *366*(6463), 346-351. doi: 10.1126/science.aaz0109

Savran, W. H., Werner, M. J., Marzocchi, W., Rhoades, D. A., Jackson, D. D., Milner, K., ... Michael, A. (2020). Pseudoprospective evaluation of UCERF3-ETAS forecasts during the 2019 Ridgecrest sequence. *Bull. Seismol. Soc. Am.*, *110*(4), 1799-1817. doi: 10.1785/0120200026

Schorlemmer, D., Gerstenberger, M. C., Wiemer, S., Jackson, D. D., & Rhoades, D. A. (2007). Earthquake likelihood model testing. *Seismol. Res. Lett.*, *78*(1), 17-29. doi: 10.1785/gssrl.78.1.17

Schorlemmer, D., Werner, M. J., Marzocchi, W., Jordan, T. H., Ogata, Y., Jackson,

D. D., ... Zhuang, J. C. (2018). The collaboratory for the study of earthquake predictability: Achievements and priorities. *Seismol. Res. Lett.*, *89*(4), 1305-1313. doi: 10.1785/0220180053

SCSN. (2020). *Southern California Seismic Network.* `https://service.scedc.caltech.edu/eq-catalogs/date\_mag\_loc.php`. (last accessed: 2020-12-01) doi: 10.7909/C3WD3xH1

Shcherbakov, R., Goda, K., Ivanian, A., & Atkinson, G. M. (2013). Aftershock statistics of major subduction earthquakes. *Bull. Seismol. Soc. Am.*, *103*(6), 3222-3234. doi: 10.1785/0120120337

Shcherbakov, R., Nguyen, M., & Quigley, M. (2012). Statistical analysis of the 2010 Mw 7.1 Darfield earthquake aftershock sequence. *New Zealand J. Geol. Geophys.*, *55*(3), 305-311. doi: 10.1080/00288306.2012.676556

Shcherbakov, R., & Turcotte, D. L. (2004). A modified form of Båth's law. *Bull. Seismol. Soc. Am.*, *94*(5), 1968-1975. doi: 10.1785/012003162

Shcherbakov, R., Turcotte, D. L., & Rundle, J. B. (2004). A generalized Omori's law for earthquake aftershock decay. *Geophys. Res. Lett.*, *31*(11), L11613. doi: 10.1029/2004GL019808

Shcherbakov, R., Turcotte, D. L., & Rundle, J. B. (2005). Aftershock statistics. *Pure Appl. Geophys.*, *162*(6-7), 1051-1076. doi: 10.1007/s00024-004-2661-8

Shcherbakov, R., Turcotte, D. L., & Rundle, J. B. (2006). Scaling properties of the Parkfield aftershock sequence. *Bull. Seismol. Soc. Am.*, *96*(4B), S376-384. doi: 10.1785/0120050815

Shcherbakov, R., Turcotte, D. L., & Rundle, J. B. (2015). Complexity and earthquakes. In H. Kanamori (Ed.), *Earthquake seismology* (2nd ed., Vol. 4, p. 627-653). Elsevier.

Shcherbakov, R., Yakovlev, G., Turcotte, D. L., & Rundle, J. B. (2005). Model for the distribution of aftershock interoccurrence times. *Phys. Rev. Lett.*, *95*, 218501. doi: 10.1103/PhysRevLett.95.218501

Shcherbakov, R., Zhuang, J., & Ogata, Y. (2018). Constraining the magnitude of the largest event in a foreshock-mainshock-aftershock sequence. *Geophys. J. Int.*, *212*(1), 1-13. doi: 10.1093/gji/ggx407

Shcherbakov, R., Zhuang, J., Zöller, G., & Ogata, Y. (2019). Forecasting the magnitude of the largest expected earthquake. *Nat. Commun.*, *10*, Art. 4051. doi:

10.1038/s41467-019-11958-4

Shearer, P. M. (2012). Self-similar earthquake triggering, Båth's law, and foreshock/aftershock magnitudes: Simulations, theory, and results for southern California. *J. Geophys. Res.*, *117*, B06310. doi: 10.1029/2011jb008957

Shebalin, P., Narteau, C., & Baranov, S. V. (2020). Earthquake productivity law. *Geophys. J. Int.*, *222*(2), 1264-1269. doi: 10.1093/gji/ggaa252

Shebalin, P., Narteau, C., Holschneider, M., & Schorlemmer, D. (2011). Short-term earthquake forecasting using early aftershock statistics. *Bull. Seismol. Soc. Am.*, *101*(1), 297-312. doi: 10.1785/0120100119

Tahir, M., Grasso, J. R., & Amorese, D. (2012). The largest aftershock: How strong, how far away, how delayed? *Geophys. Res. Lett.*, *39*, L04301. doi: 10.1029/2011gl050604

Taroni, M., Marzocchi, W., Schorlemmer, D., Werner, M. J., Wiemer, S., Zechar, J. D., ... Euchner, F. (2018). Prospective CSEP evaluation of 1-day, 3-month, and 5-yr earthquake forecasts for Italy. *Seismol. Res. Lett.*, *89*(4), 1251-1261. doi: 10.1785/0220180031

Tinti, S., & Mulargia, F. (1987). Confidence intervals of *b*-values for grouped magnitudes. *Bull. Seismol. Soc. Am.*, *77*(6), 2125-2134.

Toda, S., & Stein, R. S. (2020). Long- and short-term stress interaction of the 2019 Ridgecrest sequence and Coulomb-based earthquake forecasts. *Bull. Seismol. Soc. Am.*, *110*(4), 1765-1780. doi: 10.1785/0120200169

USGS. (2006). *U.S. Geological Survey and California Geological Survey quaternary fault and fold database.* `https://earthquake.usgs.gov/hazards/qfaults/`. (last accessed: 2020-07-01)

Utsu, T. (1961). A statistical study on the occurrence of aftershocks. *Geophys. Mag.*, *30*, 521-605.

Utsu, T., Ogata, Y., & Matsu'ura, R. S. (1995). The centenary of the Omori formula for a decay law of aftershock activity. *J. Phys. Earth*, *43*(1), 1-33.

Vere-Jones, D. (1969). A note on the statistical interpretation of Båth's law. *Bull. Seismol. Soc. Am.*, *59*, 1535-1541.

Vere-Jones, D. (1975). Stochastic models for earthquake sequences. *Geophys. J. Int.*, *42*(2), 811-826. doi: 10.1111/j.1365-246X.1975.tb05893.x

Vere-Jones, D. (2010). Foundations of statistical seismology. *Pure Appl. Geophys.*, *167*(6-7), 645-653. doi: 10.1007/s00024-010-0079-z

Werner, M. J., Helmstetter, A., Jackson, D. D., & Kagan, Y. Y. (2011). High-resolution long-term and short-term earthquake forecasts for California. *Bull. Seismol. Soc. Am.*, *101*(4), 1630-1648. doi: 10.1785/0120090340

Zechar, J. D., Gerstenberger, M. C., & Rhoades, D. A. (2010). Likelihood-based tests for evaluating space-rate-magnitude earthquake forecasts. *Bull. Seismol. Soc. Am.*, *100*(3), 1184-1195. doi: 10.1785/0120090192

Zöller, G., Holschneider, M., & Hainzl, S. (2013). The maximum earthquake magnitude in a time horizon: Theory and case studies. *Bull. Seismol. Soc. Am.*, *103*(2A), 860-875. doi: 10.1785/0120120013

Supporting Information for: "Statistics and Forecasting of Aftershocks during the 2019 Ridgecrest, California, Earthquake Sequence"

Robert Shcherbakov[1,2] *

[1]Department of Earth Sciences, University of Western Ontario, London, Ontario, *N6A 5B7*, Canada.

[2]Department of Physics and Astronomy, University of Western Ontario, London, Ontario, *N6A 3K7*, Canada.

Contents of this file

1. Figures S1 to S16
2. Tables S1 to S3

*E-mail: rshcherb@uwo.ca

Introduction

The Supporting Information for this article includes Tables S1-S3 with the parameters of the Gamma distribution, which was used as a prior distribution for the parameters of the three models considered in the work. It also includes plots illustrating the fit of the compound OU (Figure S1) and the ETAS (Figure S2) models. The MCMC sampling of the model parameters for the OU (Figures S4-S5), the compound OU (Figures S6-S8), the ETAS (Figures S9-S11) models are provided for one specific training and forecasting time intervals. The forecast evolution during 330 days after the occurrence of the M7.1 mainshock is given in Figure S12. The additional quantile scores of the plots are given in Figures S13-S16.

The data analysis was performed using computer scripts written in Matlab and can be requested from the author.

List of figures

The compound Omori-Utsu (OU) model

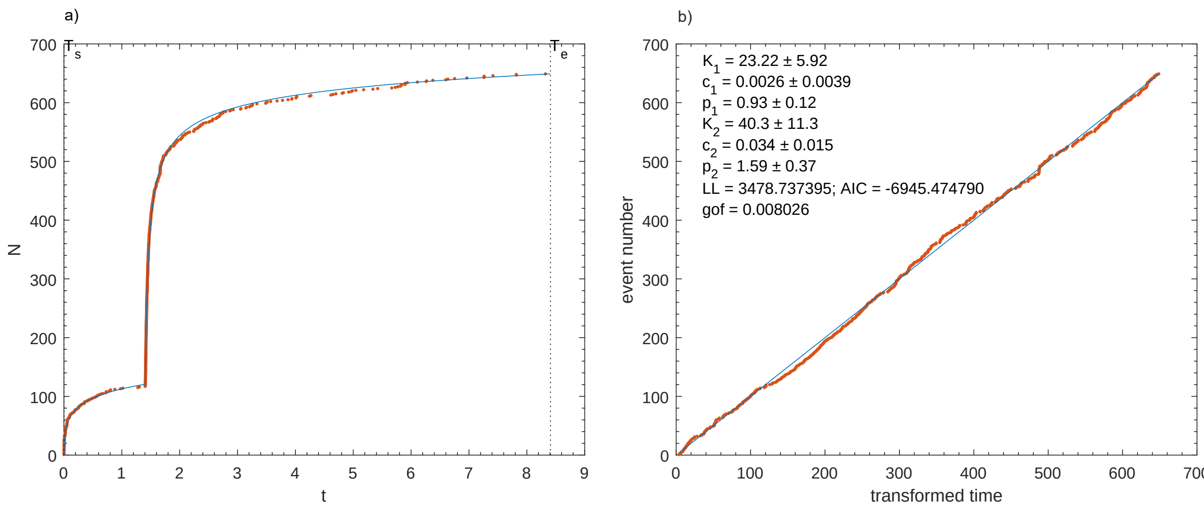

Figure S1. The fitting of the compound Omori-Utsu law, equation (5), to the 2019 Ridgecrest sequence. $T_0 = 0$ corresponds to the occurrence of M6.4 foreshock on 2019/07/04 (17:33:49 UTC). a) The cumulative number of earthquakes is plotted as solid symbols. The corresponding fit of the compound Omori-Utsu law to the cumulative numbers is given as solid curve during the time interval $[T_0, T_e] = [0, 8.407]$ days. This includes 7 days of aftershocks after the M7.1 mainshock. b) The number of earthquakes is plotted in transformed time. All earthquakes above magnitude $m \geq 3.2$ were used.

The Epidemic Type Aftershock Sequence (ETAS) model

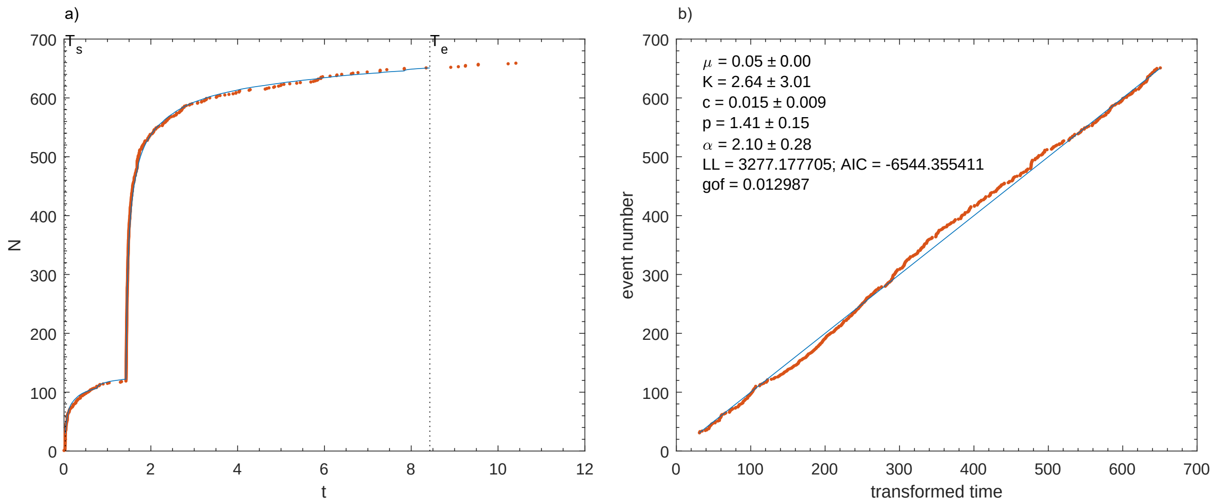

Figure S2. The fitting of the ETAS model, equation (6), to the 2019 Ridgecrest sequence. $T_0 = 0$ corresponds to the occurrence of M3.98 foreshock on 2019/07/04 (17:02:55 UTC). a) The cumulative number of earthquakes is plotted as solid symbols. The corresponding fit of the ETAS model to the cumulative numbers is given as solid curve during the time interval $[T_s, T_e] = [0.03, 8.428]$ days. This includes 7 days of aftershocks after the M7.1 mainshock. b) The number of earthquakes is plotted in transformed time. All earthquakes above magnitude $m \geq 3.2$ were used.

Markov Chain Monte Carlo sampling

The Omori-Utsu (OU) model parameters

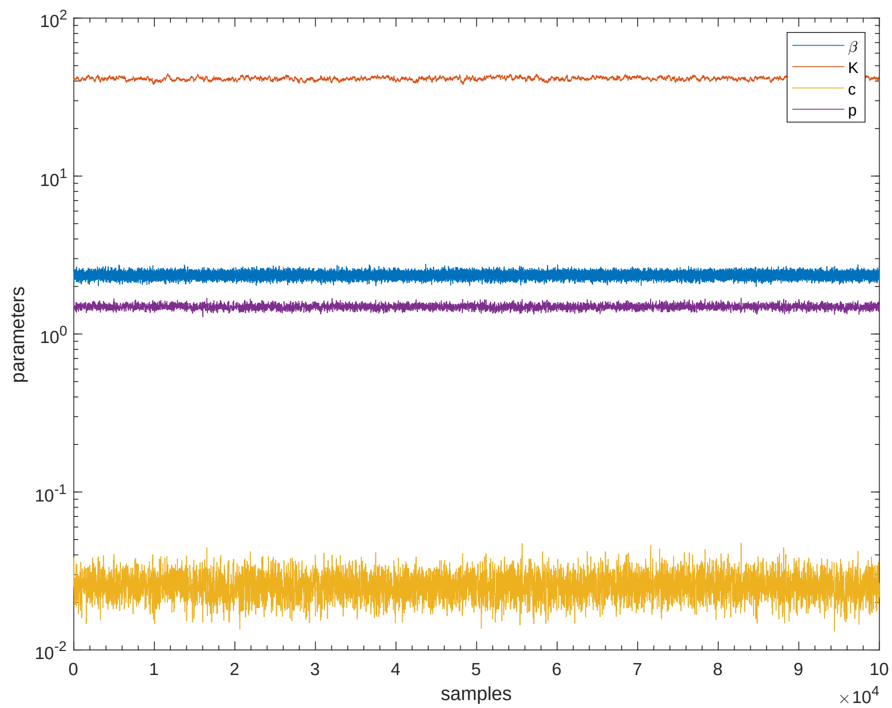

Figure S3. The MCMC chains of the OU model parameters sampled from the posterior distribution for the Ridgecrest sequence during one day of aftershocks above magnitude $m_c = 3.2$ and starting from the occurrence of the M7.1 mainshock. The total number of MCMC 200,000 steps were generated and 100,000 steps were discarded as burn-in.

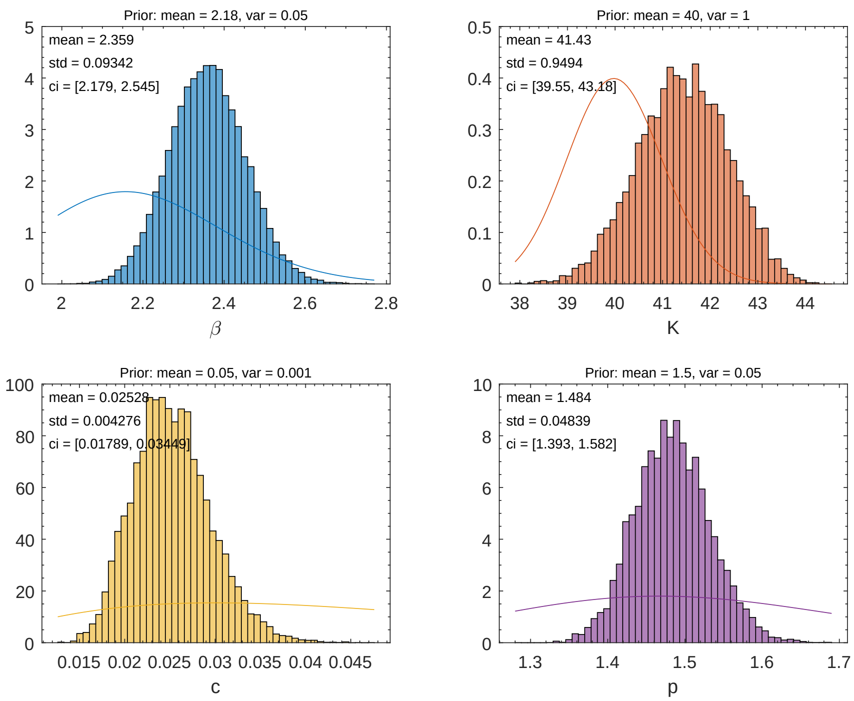

Figure S4. The distribution of the OU model parameters computed from the MCMC chains given in Figure S3. The corresponding mean, standard deviation, and 95% Bayesian confidence bounds for the parameters are provided in the legend. The solid curves represent the prior Gamma distribution for each model parameter.

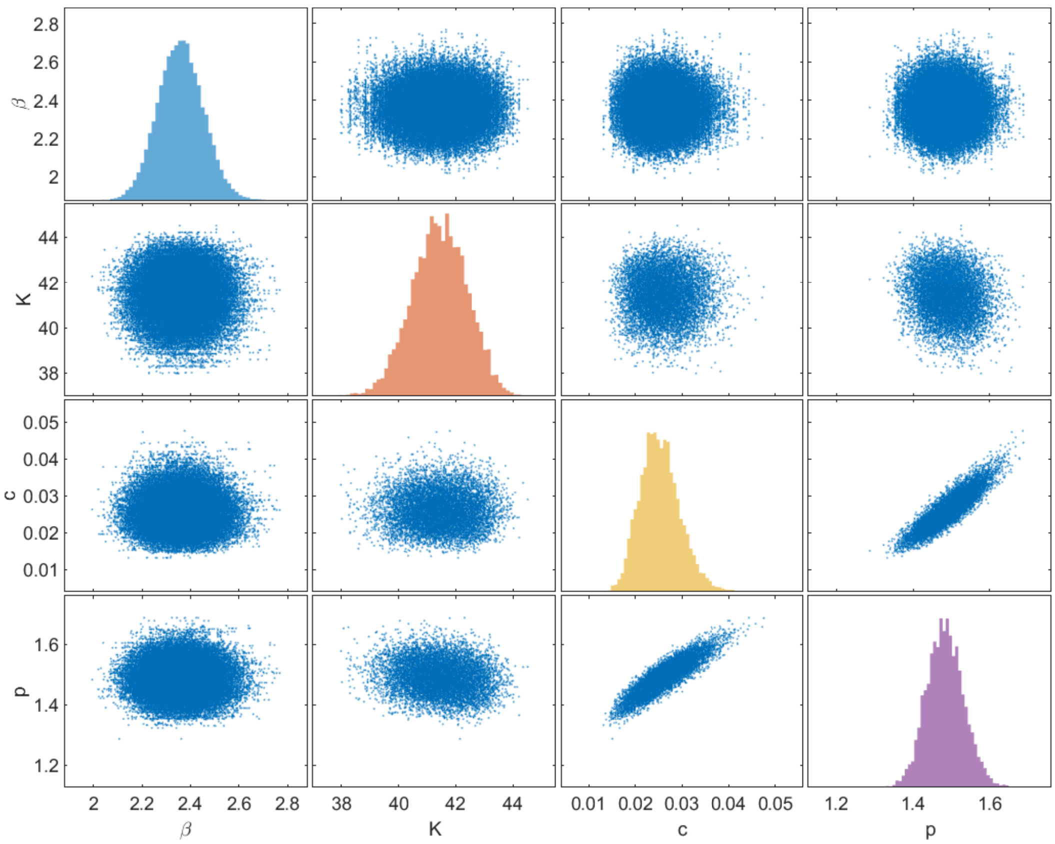

Figure S5. The matrix plot of the pairs of the OU model parameters computed from the MCMC chains given in Figure S3 and showing the correlation structure of the parameters.

The compound OU model parameters

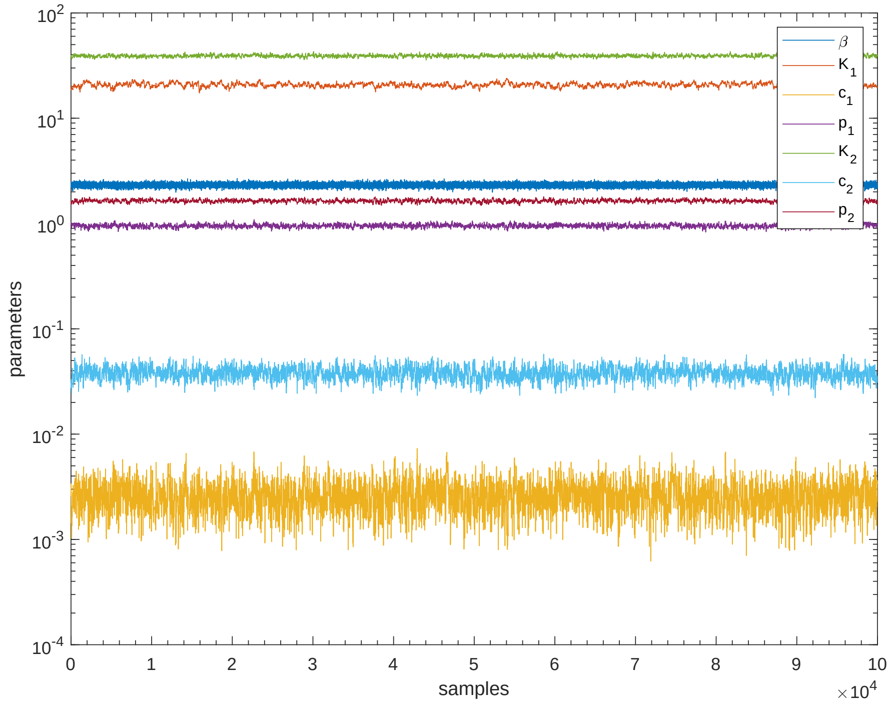

Figure S6. The MCMC chains of the compound OU model parameters sampled from the posterior distribution for the Ridgecrest sequence during $[T_0, T_e] = [0, 2.407]$ target time interval with aftershocks above magnitude $m_c = 3.2$ and starting from the occurrence of the M6.4 foreshock. The total number of MCMC 200,000 steps were generated and 100,000 steps were discarded as burn-in.

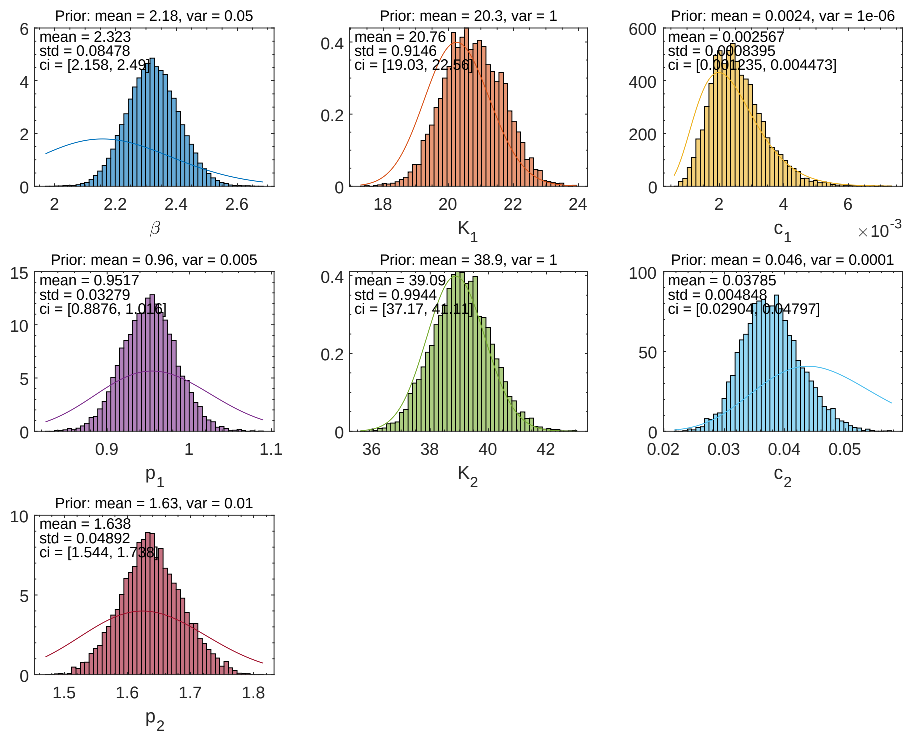

Figure S7. The distribution of the compound OU model parameters computed from the MCMC chains given in Figure S6. The corresponding mean, standard deviation, and 95% Bayesian confidence bounds for the parameters are provided in the legend. The solid curves represent the prior Gamma distribution for each model parameter.

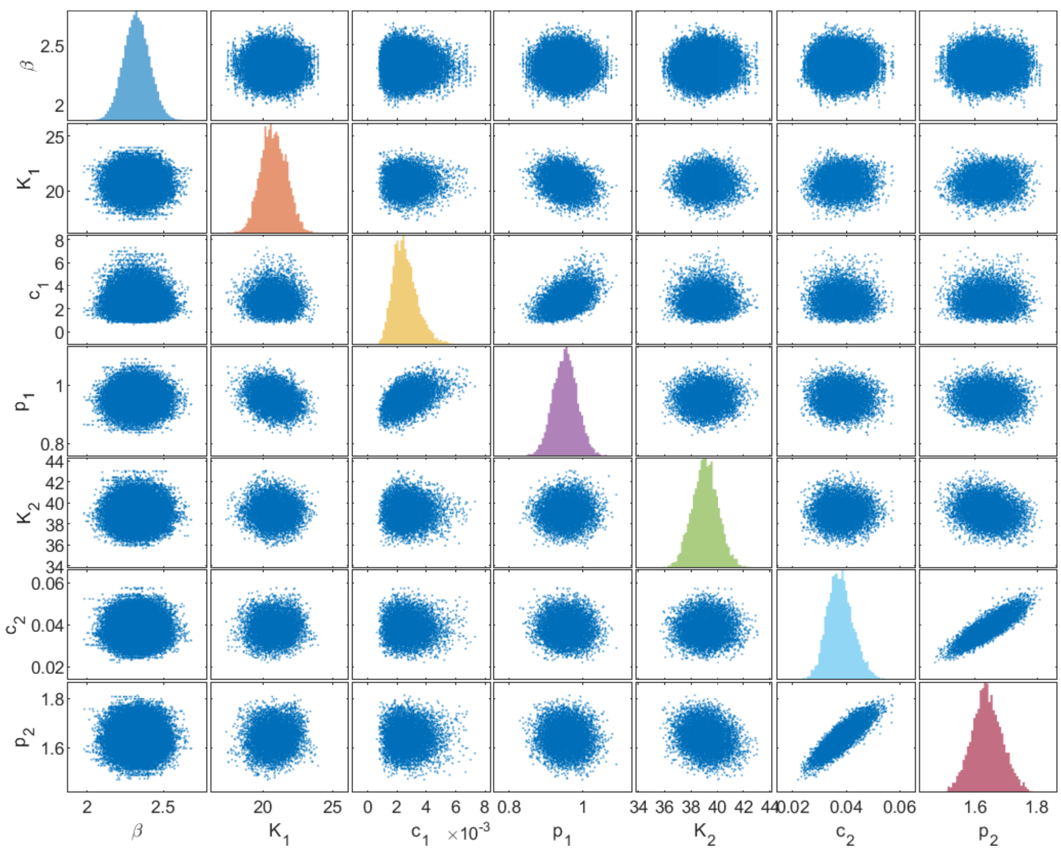

Figure S8. The matrix plot of the pairs of the compound OU model parameters computed from the MCMC chains given in Figure S6 and showing the correlation structure of the parameters.

The ETAS model parameters

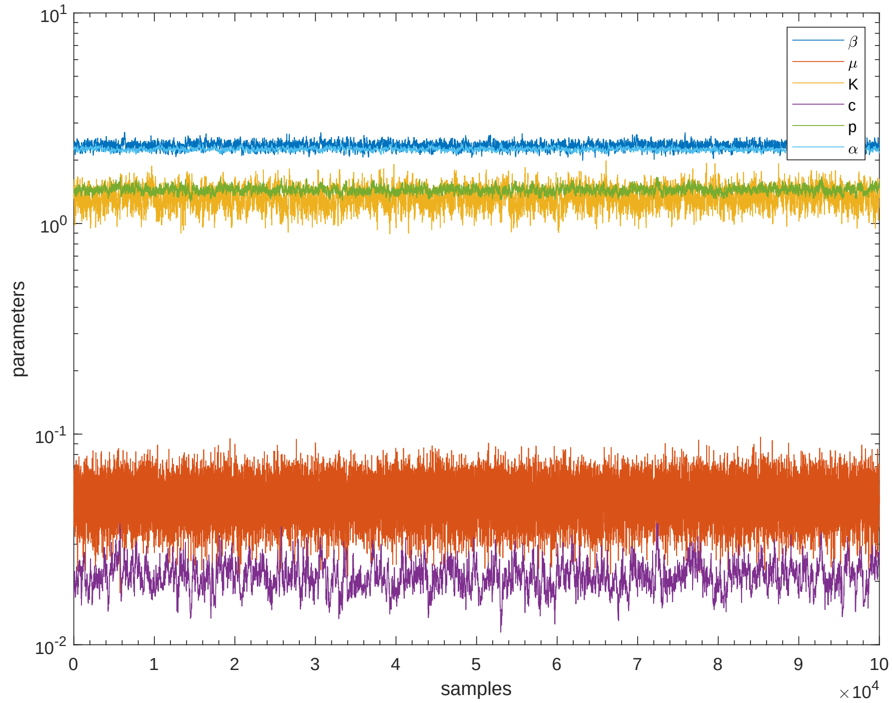

Figure S9. The MCMC chains of the ETAS parameters sampled from the posterior distribution for the 2019 Ridgecrest sequence $[T_s, T_e] = [0.03, 2.428]$ target time interval with aftershocks above magnitude $m_c = 3.2$ and starting from the occurrence of the M6.4 foreshock. The total number of 150,000 steps were generated and 50,000 steps were discarded as burn-in.

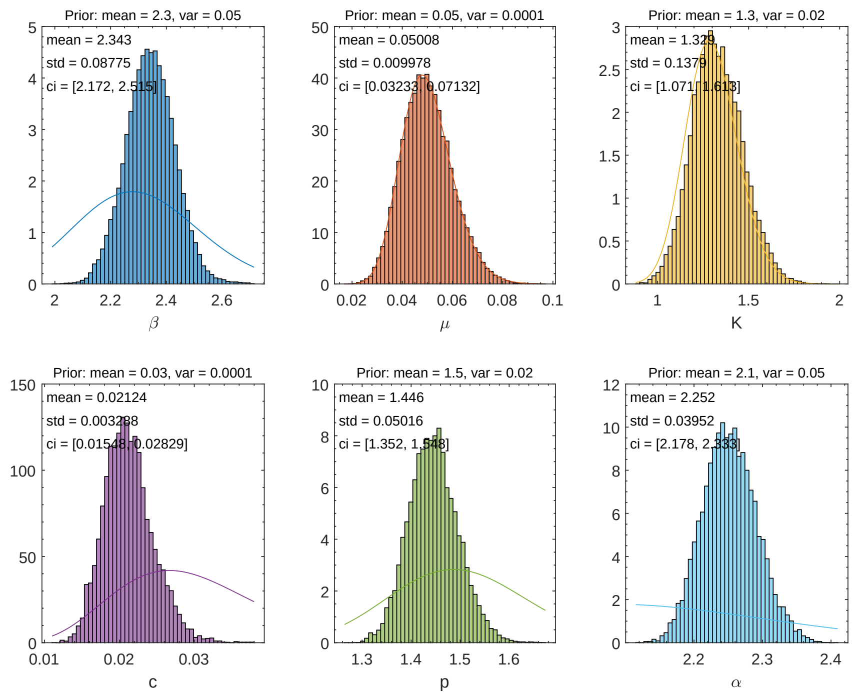

Figure S10. The distribution of the ETAS parameters computed from the MCMC chains given in Figure S9. The corresponding mean, standard deviation, and 95% Bayesian confidence bounds for the parameters are provided in the legend. The solid curves represent the prior Gamma distribution for each model parameter.

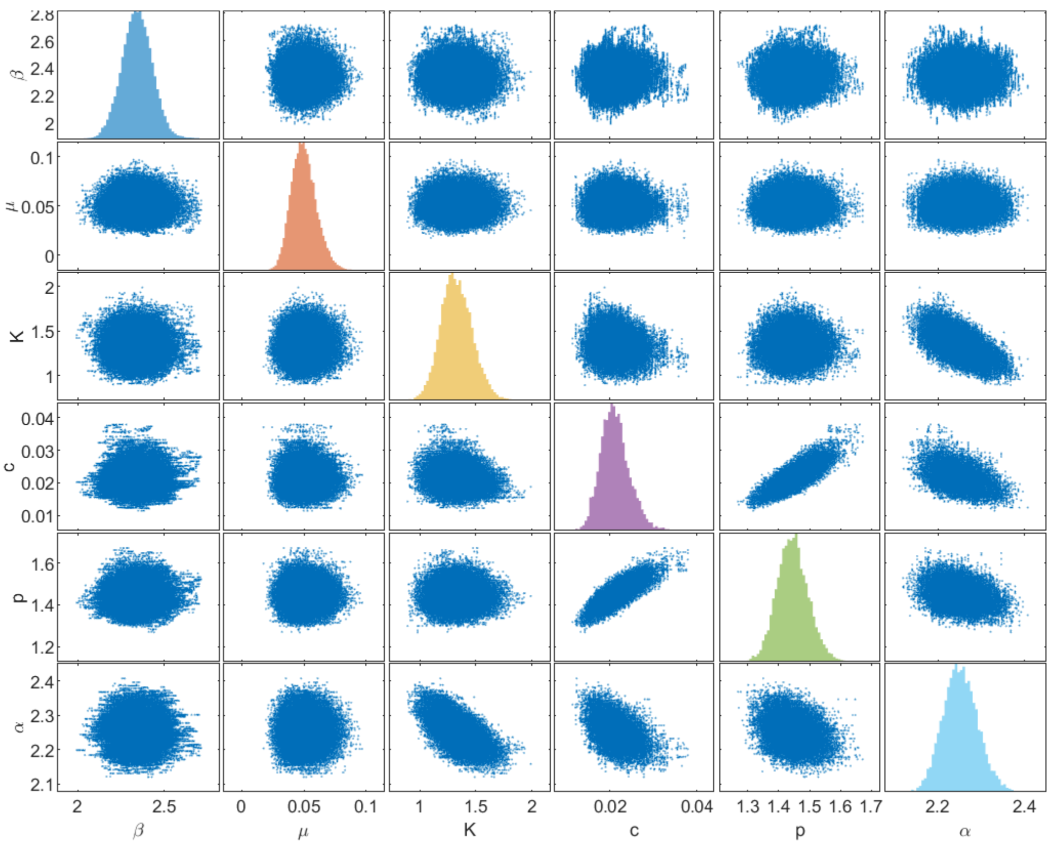

Figure S11. The matrix plot of the pairs of the ETAS parameters computed from the MCMC chains given in Figure S9 and showing the correlation structure of the simulated parameters.

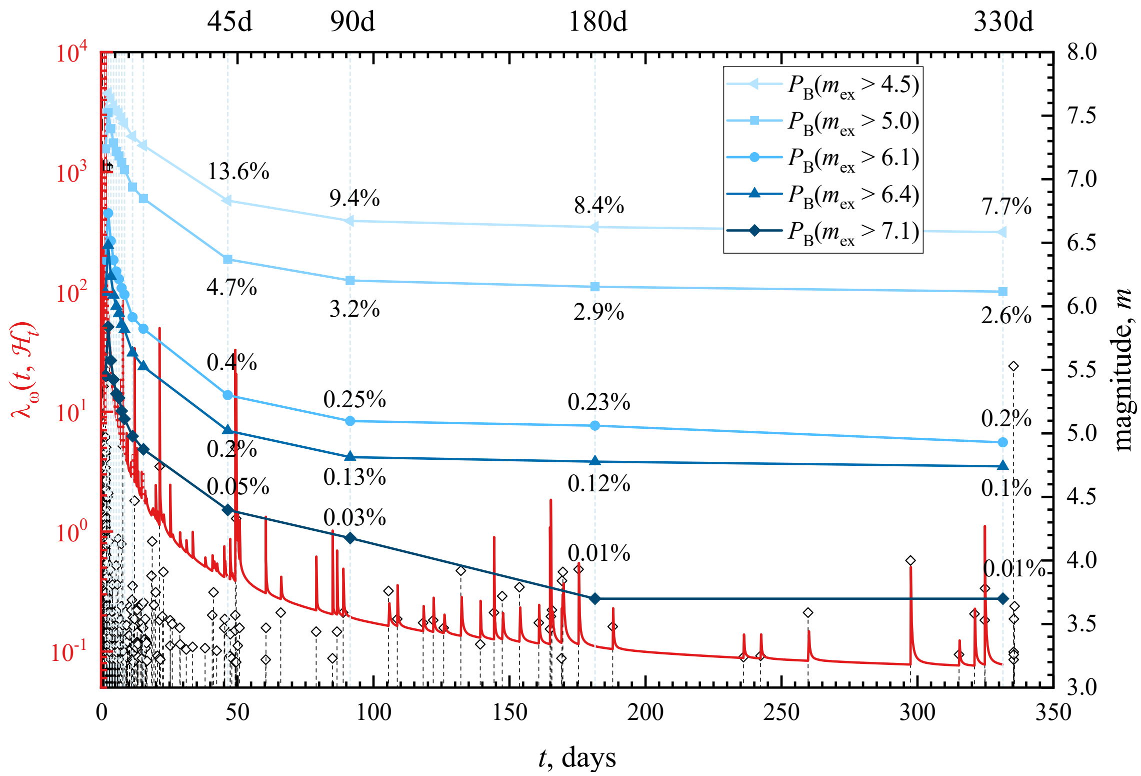

Figure S12. The probabilities for the largest expected earthquake to be above the magnitudes $m_{\text{ex}} \geq 4.5$, 5.0, 6.1, 6.4, 7.1 and during the progressively increasing time intervals since 2019/07/04 (17:02:55 UTC). The probabilities are estimated using the BPD combined with the ETAS model for the earthquake rate during the forecasting time interval $\Delta T = 7$ days and plotted in a logarithmic scale. The earthquake magnitudes of the 2019 Ridgecrest sequence are plotted as open diamonds for all events above magnitude $m \geq 3.2$. The fit of the ETAS model is shown as a solid curve.

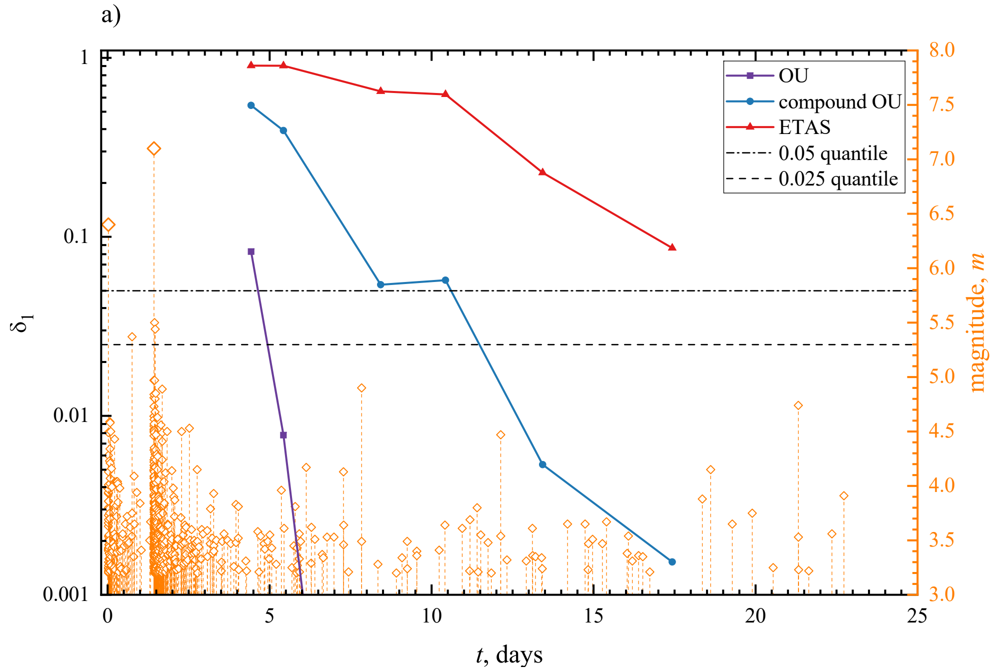

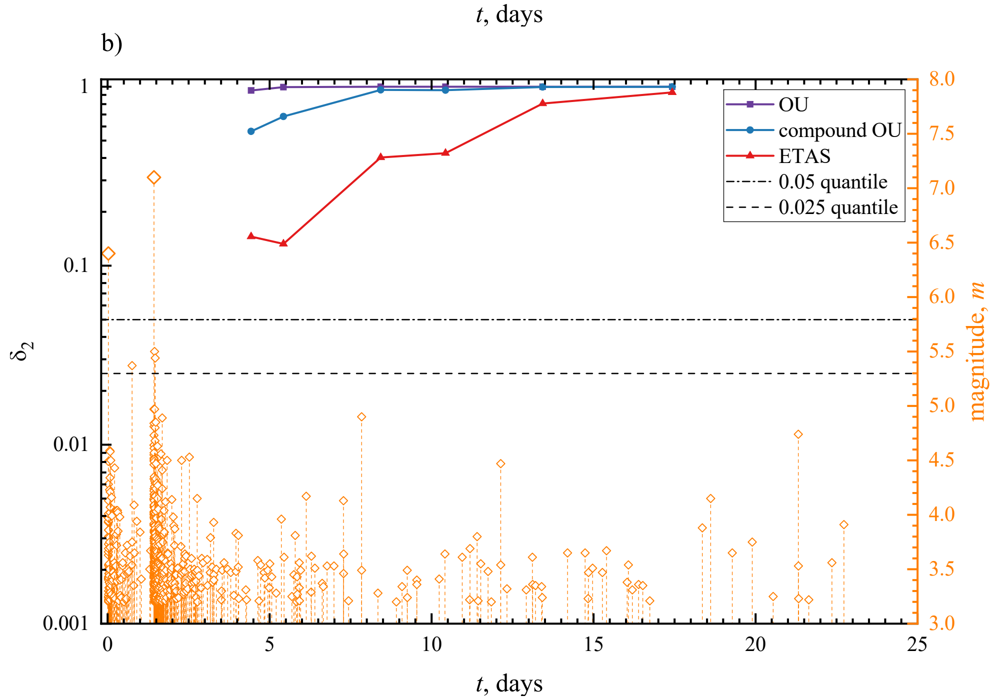

Figure S13. Plot of the quantile scores a) δ_1 (N-test), b) δ_2 (N-test), and c) κ (M-test) for the performance of the aftershock forecasts based on the three point process models. The scores are computed at the end of each forecasting time interval. The end of the training time interval is fixed at $T_e = 3.428$ days while the forecasting time interval is increasing as $\Delta T = 1, 2, 5, 7, 10, 14$.

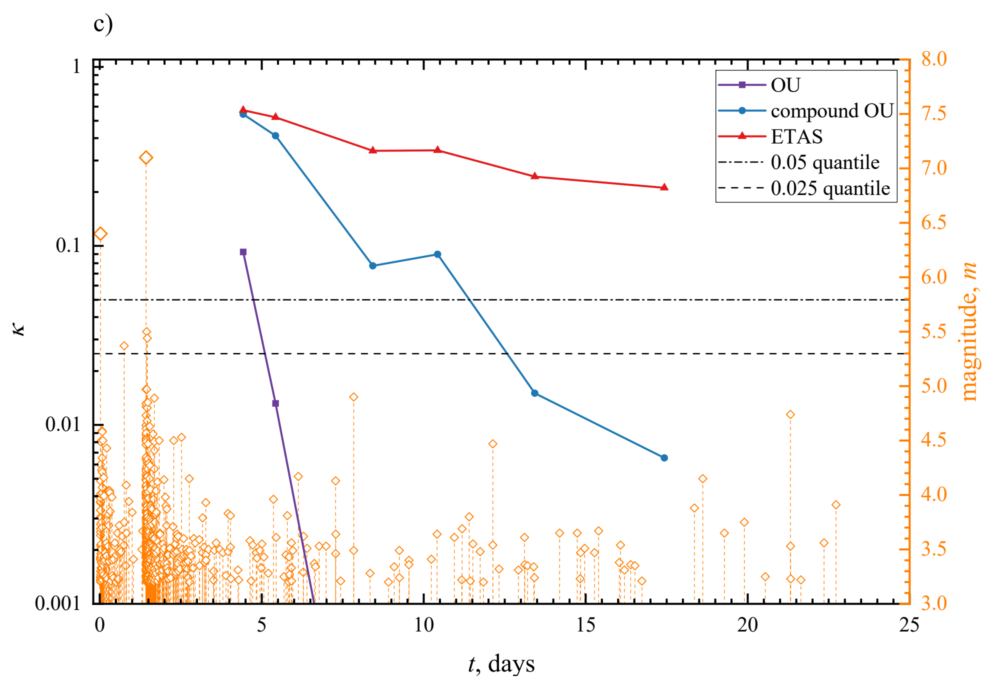

Figure S13. Continued.

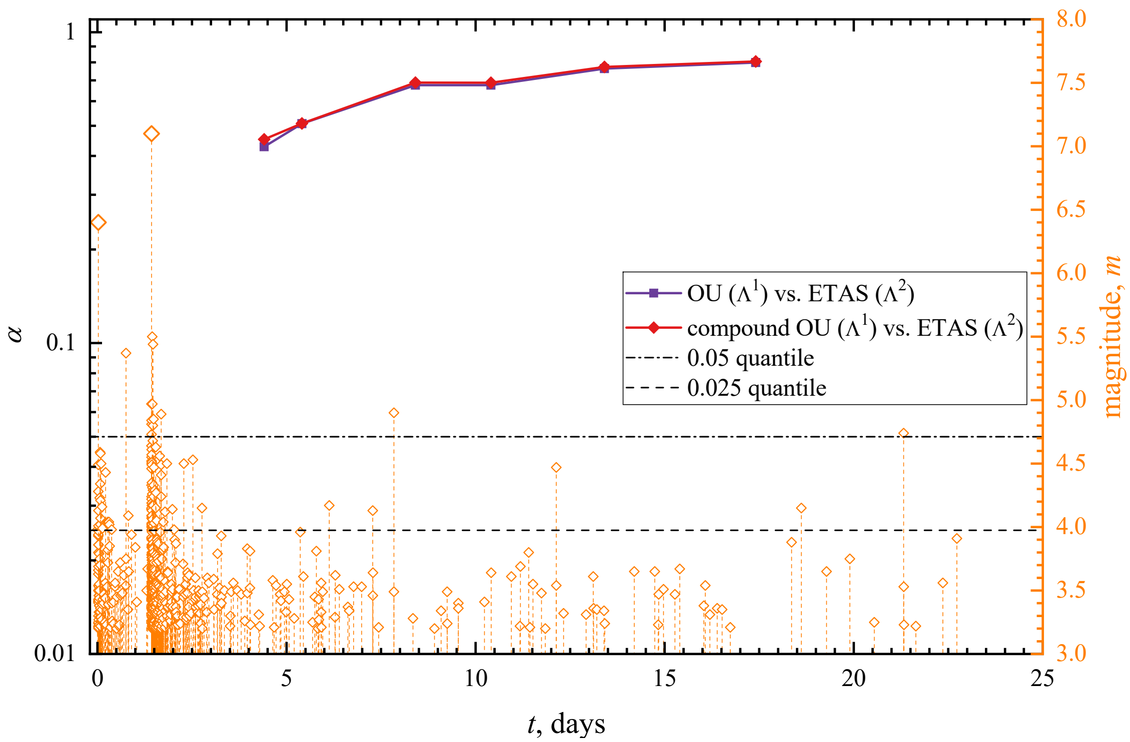

Figure S14. Plot of the quantile score α (R-test) for the comparative test of the ETAS model versus the forecast based on the OU model and on the compound OU model. The scores are computed at the end of each forecasting time interval as in Figure S13.

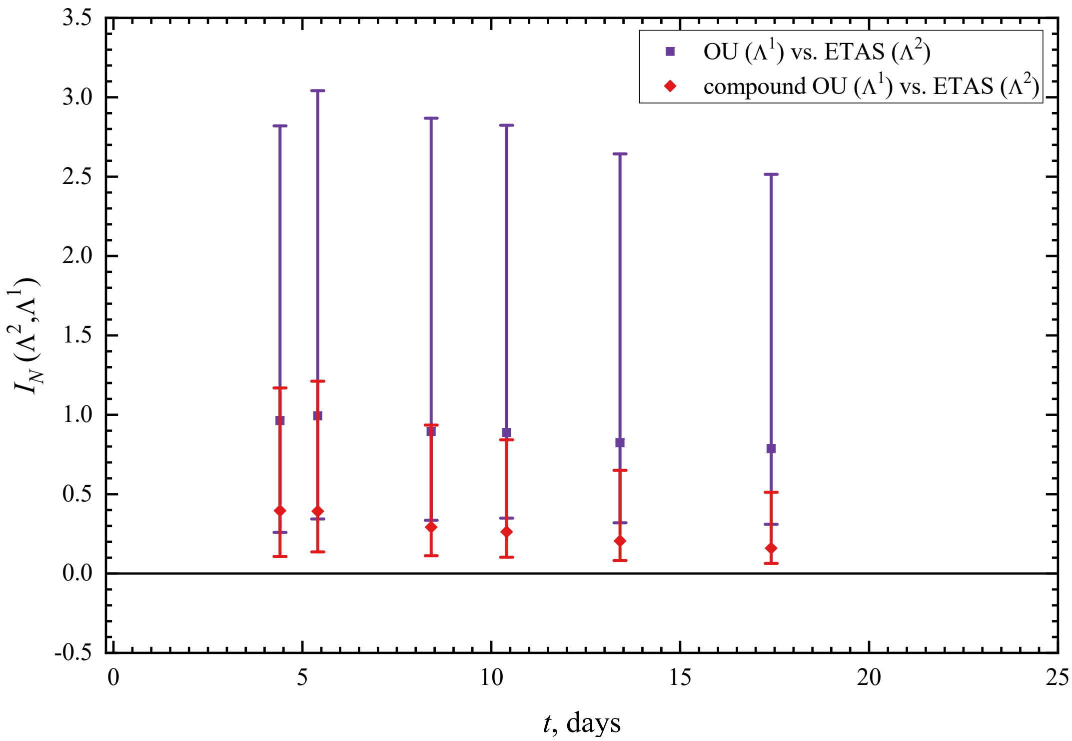

Figure S15. The sample information gain for the pairs of the models. The solid squares correspond to the comparison of the forecasts based on the ETAS model versus the forecasts based on the OU model. The solid diamonds correspond to the comparison of the forecasts based on the ETAS model versus the forecast based on the compound OU model. The 95% confidence intervals are given.

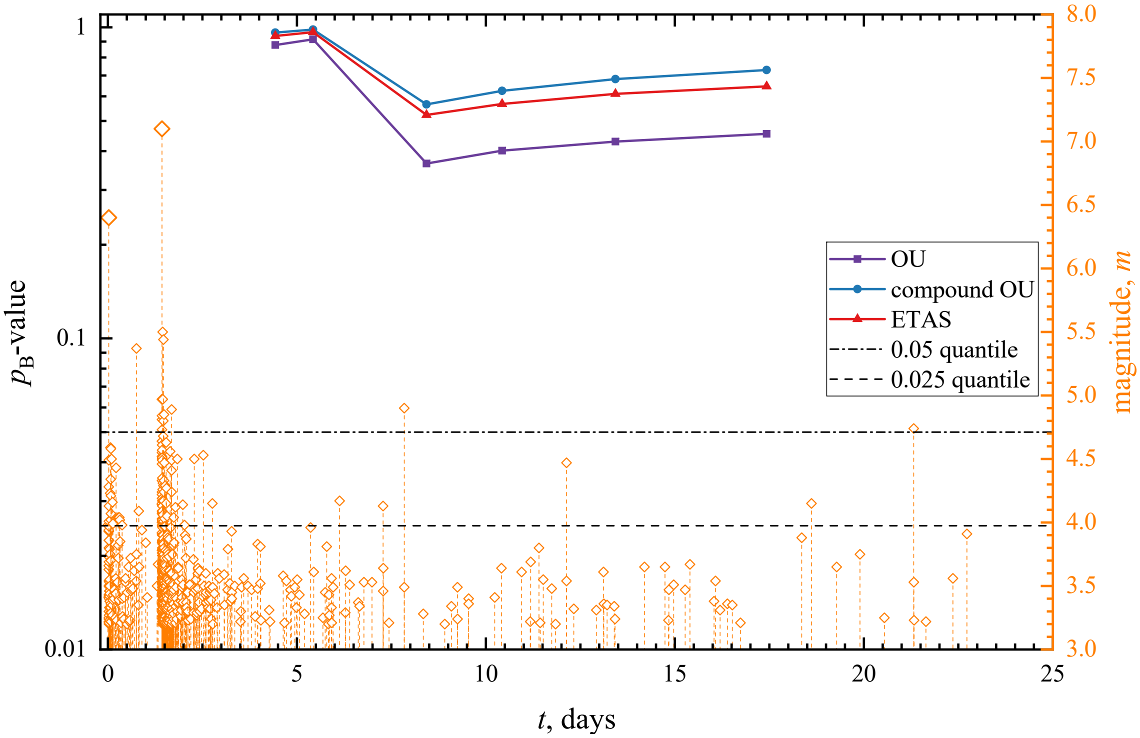

Figure S16. Plot of the Bayesian predictive distribution p-value for the three models. The p-values are computed at the end of each forecasting time interval as in Figure S13.

Tables for the model prior parameters

The Omori-Utsu model

Table S1. Summary of the parameters used for the prior distribution of the OU model $\{\theta, \omega\} = \{\beta, K_o, c_o, p_o\}$. For the priors $\pi(\{\theta, \omega\})$ the Gamma distribution was used with the mean and variance specified for each parameter.

Prior for	β	K_o	c_o	p_o
mean	2.18	40.0	0.05	1.5
Var	0.05	1.0	1e-3	0.05

The compound Omori-Utsu model

Table S2. Summary of the parameters used for the prior distribution of the compound OU model $\{\theta, \omega\} = \{\beta, K_1, c_1, p_1, K_2, c_2, p_2\}$. For the priors $\pi(\{\theta, \omega\})$ the Gamma distribution was used with the mean and variance specified for each parameter.

Prior for	β	K_1	c_1	p_1	K_2	c_2	p_2
mean	2.18	20.3	0.0024	0.96	38.9	0.046	1.63
Var	0.05	1.0	1e-6	0.005	1.0	1e-4	0.01

The Epidemic Type Aftershock Sequence (ETAS) model

Table S3. Summary of the parameters used for the prior distribution of the ETAS model $\{\theta, \omega\} = \{\beta, \mu, K, c, p, \alpha\}$. For the priors $\pi(\{\theta, \omega\})$ the Gamma distribution was used with the mean and variance specified for each parameter.

Prior for	β	μ	K	c	p	α
mean	2.3	0.05	1.3	0.03	1.5	2.1
Var	0.05	1e-4	0.02	1e-4	0.02	0.05